

Point-to-point reply to reviewers

Paper was-2025-120

Title:

Large Eddy Simulation of the IEA 15-MW Wind Turbine Using a Two-Way Coupled Fluid-Structure Interaction Model

December 12, 2025

The authors wish to thank the reviewers for their comments and suggestions on the paper to enhance the manuscript. The paper has been revised accordingly. The revised parts have been highlighted in blue (for this referee) and red (for referee 1) in the updated manuscript. If mentioned, the page number refers to the revised paper. In the following we report point-to-point replies concerning the questions and comments raised by the reviewers.

Reviewer #2

Main Critique Points

1. *The term "aeroelasticity" is well known, I suggest removing this definition.*

We have eliminated this sentence.

2. *Strictly speaking, fatigue itself is not an aeroelastic phenomenon, but aeroelastic effects can cause or accelerate fatigue in wind turbines.*

We have specified that in the text. The referee can find the revised version of the manuscript attached and follow the text in blue.

3. *I suggest to slightly rephrase this sentence, softening it. I agree with the authors that BEM aerodynamics has significant limitations. Anyhow, it is currently the state-of-the-art solvers for practical industrial applications and certification. Moreover, beside highlighting its limitations, several works have demonstrated that, if properly tuned, it can be a valuable engineering-type solver, complementary to higher fidelity ones which have also higher computational costs. See, for instance, the results of IEA WIND Task 47..*

We have restated the text in this paragraph, and cited the references reported by the referee.

4. *I don't agree with this point of view. It is true that panel methods (and in general potential flow solvers and/or free-vortex wake methods) and ALM solvers are computationally more expensive than BEM. Nevertheless, they are less expensive than blade-resolved CFD. Furthermore, many papers show that panel codes and free-wake vortex methods are able to capture unsteady blade/rotor aerodynamics with good accuracy in different operating conditions (including off-design) whenever massive flow separation phenomena do not occur. See, for instance:..*

We have restated the text in this paragraph, and cited the references reported by the referee.

5. *From this sentence it appears that CFD is described as the best compromise between accuracy and computational costs. Differently, within the research topic addressed in this work, CFD should be seen as the reference high-fidelity approach that can be used for a (limited) number of computations in order to refine and/or assess the lower fidelity models.*

We agree with the referee and we have restated the text in this part.

6. *This sentence is not clear. The paragraph describes tools such as FAST which is not based on a lifting-line aerodynamic formulation.*

Sorry it was meant to be "BEM" instead of lifting line. We have corrected that in the text.

7. *At this point is not clear if, within the aeroelastic computation, the ALM elements follow blade deformation or not.*

We have now specified that the ALM elements do not follow the blade deformation.

8. *Please provide more details about the procedure used to compute the flow velocity contribution to u_{rel} . Which approach was used (Line Averaging Technique, for instance, or others?).*

The definition of u_{rel} is given in eq. (7). The interpolation from the structural FEM nodes for u_{def} to the Cartesian CFD mesh on which u_{abs} is defined, is made with a simple linear interpolation. Then, the resulting u_{rel} is interpolated on the nodes discretizing the blade.

9. *Although the authors refer to previous works for the structural model, it is preferable to briefly outline it here. Which type of beam model is used (Euler-Bernoulli, Timoshenko, others)? Is it a linear model or a nonlinear one? Are the Coriolis forces and the spin-softening effect taken into account?*

We have now specified that it is a linear model taking into account Coriolis, centrifugal and Euler effects. Concerning the type of beam model (Euler-Bernoulli), it is specified in the text under eq. 6.

10. *Please indicate if the modal analysis is performed on the rotating or nonrotating blade. In the latter case, is it performed past the deformed or undeformed configuration?*

We have now specified this at several points in the paper.

11. *The authors state that they are using a modal approach to solve the aeroelastic equations. How is the Lumped Mass representation here mentioned linked to the modal approach? As a general comment, in my opinion the description of the structural model is not clear and lacks suitable clarifications*

Following the approach of Reschke (2005) and Saltari et al. (2017), the inertial coupling terms arising from the noninertial frame of reference are described using a reduced set of coefficients, which are estimated via finite element method discretization. Details can be found for the specific case of wind turbine's blades in Della Posta et al. (2022). The lumped mass representation has thus been used to define the mass matrix of the blade, to evaluate the inertial coupling terms according to the mentioned method, and also as an input of the eigenproblem providing the natural frequencies and modes used in the work.

Also, we have considerably changed and extended the description of the structural model.

12. *Usually in modal approaches, the quantity d includes, for each blade section, flap (w), lag (v) and torsion (θ) DOFs. Consistently, also w' and v' will appear in the aeroelastic equations, so they will be computed as part of the aeroelastic solution. It is not clear to me*

why the torsion angle is here accounted for in addition to d .

Flap and lag are indeed considered in the structural dynamics solver, and their time derivatives are considered in the definition of the relative velocity in equation 7 as \mathbf{u}_{def} , which is defined on the basis of the translational contributions of $\dot{\mathbf{d}}$ only, as clarified now in the text. As explained after equation 8, $v_2 = \mathbf{u}_{def} \cdot \mathbf{E}_2$ is the flapwise deformation velocity component, and $v_3 = \mathbf{u}_{def} \cdot \mathbf{E}_3$ is the edgewise deformation velocity component, indicating the translational structural dynamics. The torsion is also considered as part of the elastic state relevant for the aeroelastic coupling, in order to take into account angular deformations that change the actual orientation of the local airfoil on the deformed blade with respect to the impinging flow.

13. *What do you mean by "bendings"?*

Bendings here indicate rotations around X_2 and X_3 , which describe the edgewise and flapwise (in-/out-of-plane) angular deformations respectively.

14. *It is important to provide an indication of the computational costs of a typical solution.*

The increase in computational cost induced by the structural solver is negligible, as it accounts for less than 2%.

15. *Please describe how this is computed, as it is one of the critical aspects of ALM methods.*

Please, see answer to comment number 8 of the present referee.

16. *I am confused by the appearance of $_{tors}$ here. If I understood correctly, the modal dofs already include both bending (flap and lag) and torsion. Please clarify.*

As now mentioned in the revised methodology, once the modal dynamics is advanced in time, the displacement is projected back onto the physical base to recover its expression in the rotating frame of reference. We have also explicitly explained in the revised manuscript that \mathbf{u}_{def} only considers the time derivative of the translational degrees of freedom, so that the presence of $_{tors}$ should be clearer in eq.8.

17. *OpenFAST is a widely used tool, so, in my opinion, there is no need to devote a specific section to its description. I suggest that simply specifying the main characteristics of the aerodynamic and structural formulation (sepcifically indicating if blade torsion has been included or not - i.e. if BeamDyn or Elastodyn has been used) is sufficient.*

We have now eliminated this subsection and included only a small paragraph in the next section.

18. *I presume the shear inflow is imposed at the inlet, is it correct? If so, using a no-slip condition at the bottom will modify the actual inflow at the rotor disk. Please clarify this aspect.*

We have now explained in the text that indeed the flow changes from the inflow to the turbine, but the provided profile comply with the no-slip condition.

19. *Rotating or nonrotating? Past the deformed or undeformed configuration (if rotating)?*

We have now specified that it is the rotating undeformed configuration.

20. *Is the pitching moment computed past the $c/4$ point of each blade section?*

We confirm that.

21. *I suggest changing the scale of the contour plot because it is difficult to appreciate the different TKE levels. If this is difficult considering the predicted values of TKE, it may help showing directly the TKE difference between the TN and OR case. Moreover, the figures are really small.*

We have enlarged and reorganized the figures. The slices are now presented in a single column to enhance their readability.

22. *I don't understand the values y/D indicated in the plot. If I see correctly from Fig.5 the tower base is at $y/D=0$, so why would these horizontal planes be at $y/D \neq 0$? Moreover, top panels of Fig 6 show a deviation of the hub wake from the turbine rotation axis. Something similar happens when the rotor is in yaw, but here it is not the case. It would be interesting to provide a justification for this phenomenon.*

In this figure $y=0$ was erroneously set at the hub of the turbine, we have changed that for consistency, introducing the value h_{hub} . The deviation of the hub wake from the turbine rotation axis is not due to the yaw but to the mutual effect of the asymmetry induced by the rotation of the blades and the wake meandering. Concerning the second effect, the wake is subject to low frequency oscillations, and in this snapshots it happens to be oscillating towards higher values of z , which combines positively to the slight effect towards higher values of z of the direction of rotation of the blades.

23. *Considering the number of lines in the figures it is quite difficult to recall everytime which result correspond to which line/marker. I suggest adding a graphical legend to the plots.*

Done.

24. *As a general comment to Figs 8 and 10, I suggest showing only the fluctuation of the quantities of interest, while reporting the mean values in suitable tables. As the paper is dealing with aeroelasticity, unsteady fluctuations are more interesting than the mean values. Differently, using the current plots, they are not easily appreciable.*

We have tried to plot only the fluctuations in figures 8, 10 and 12, removing the mean values, but the plot becomes very confusing since many of the lines are superposed. For completeness, we report the plot in figure 1 of the present document. This considered, we have decided not to remove the mean from the figures 8, 10, 12.

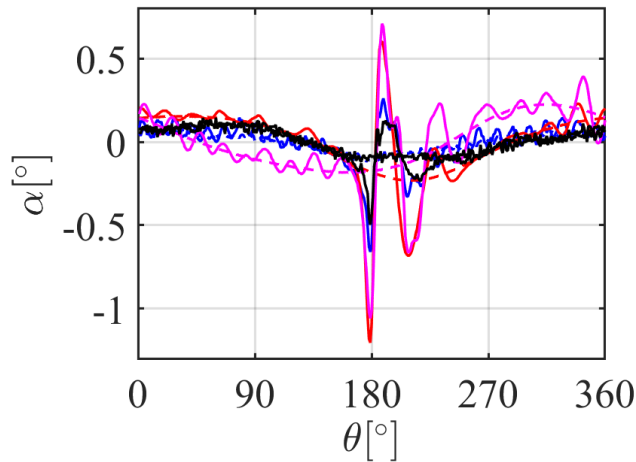


Figure 1

25. *Here flapwise and tangential force are mentioned. Before they were $F1$, $F2$. Please define a unique nomenclature for these quantities.*

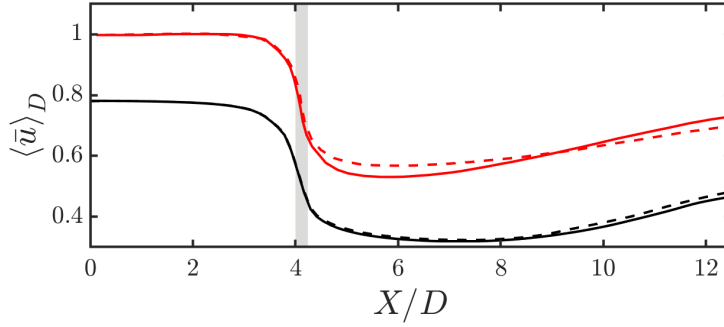


Figure 2: Rotor-averaged velocity along the streamwise direction normalized by the undisturbed velocity at the rotor height, namely, $U_\infty = 10 \text{ m/s}$, for the present data (black curves) and the work of Santoni (2017) (red curves). The grey region represents the area covered by the rotor. (RO ----, TN —).

We have now clearly defined the flapwise and edgewise forces at the end of page 12 : "flapwise and edgewise components (normal and tangential to the rotor disk), respectively, of the aerodynamic force per unit length F_2 and F_3 ". In the reminder of the paper, we now use F_2 and F_3 within the figures, and "flapwise and edgewise" in the text.

26. *This metrics is intuitively clear, but needs a formal definition.*

Done.

27. *Why are the left and right contour maps different? In addition, it would help the figure clarity if a sketch of the rotor/tower were included (maybe using transparency).*

The colormaps have been unified. Also, a sketch of the tower is now included in each subfigure.

28. *The parallel between the 5 MW and the 15 MW behaviour is very interesting and involve several aspects. Anyhow, for the sake of readability, the results related to the 5 MW which are needed to support the comments here addressed must be here reproduced. Otherwise it is quite difficult to follow the comments on the basis of the textual description of plots not shown here.*

Concerning the comparison with the 5MW turbine, as suggested by the reviewer, we have included in figure 4 of the revised paper, reported here for completeness as figure 2 of the present response, a reproduction of the nondimensionalized plot from Santoni et al. (2017) in a comparable format that allows the reader to interpret the differences more clearly. Also, we have included the results of Bernardi et al. (2023) in figure 10 of the paper. Moreover, to comply with another referee's comment, we have eliminated some further comparison with the 5MW turbine results.

29. *Which comparative 5 MW-15 MW result support this conclusion? An explicit comparison of the mentioned results is needed here.*

We have now included the curve of the figure 3 of Bernardi et al. 2023 in which it can be clearly seen that the presence of the tower induces larger oscillations in the power coefficient. However, since the inflow was different in this literature case, we have restated the sentence as: "Moreover, the present results predict that, for very large rotors and a sheared inflow, the tower effect on blade deformations is less pronounced than for smaller rotors".

30. *Indicating the value of frot would help the readability.*

We have now reported this value.

31. *Although well known, a formal definition of 1P, 2P and so on is needed.*

Done.

32. *Considering the combination of frequencies experienced by the rotor, the expected result in terms of thrust and power (both axial loads) is that only the multiple of blade passage frequency are retained in the PSD (so 3P, 6P and so on). This is actually confirmed by all proposed solvers here, except Beamdyn, which shows a significant peak at 1P. The authors should comments and justify this unexpected finding.*

We appreciate the reviewer’s observation regarding the presence of a peak at 1P in the spectra of the power and thrust coefficients for the BeamDyn-only configuration.

The presence of this peak may be likely explained by the fact that the baseline configuration of the wind turbine used in our simulations considers an additional degree of freedom that takes into account the mechanical connection between the blades.

We acknowledge that this aspect warrants further investigation, and we plan to examine it in more detail in future work. Nevertheless, we would like to emphasize that the amplitude of the 1P peak is several orders of magnitude smaller than the dominant spectral components at higher frequencies. As a result, its contribution to the overall system dynamics—and thus to the conclusions drawn in this study—is negligible. Therefore, while the mechanism behind this peak is of scientific interest, it does not materially affect the results presented here.

33. *This aspect is quite critical for the comparison between BEM-based and LES-based solvers. How can the authors be sure that the imposed inflow at the rotor disk between the two approaches is the same (at least to a certain extent)? An analysis of the inflow velocities on the reference blade along the azimuth angle is needed to quantify the differences in the wind incoming to the rotor. Moreover, in Task 47 many analyses have been performed (aslo by some of the authors) on how to align the inflow to BEM and to CFD (although in that case it referred to the turbulent inflow). Anyhow, I suggest to investigate if any of those methodologies can be used here to align the inflow to BEM and to CFD.*

We have indeed compared the aerodynamics of the present code with other ones in the IEA Task 47 "TURBINIA". In figure 4.25 of the report of Task 47 (Shepers et al. 2025), the differences in rotor aerodynamic modeling between different codes are highlighted by the time traces of hub height wind speed and axial wind velocity at a co-rotating probe on the turbine blade. Before comparing the rotor simulation results it was ensured that identical inflows were prescribed between the different codes. Figure 4.25 displays that the lifting line codes do not agree well with CFD ones on the hub height wind speed and the axial wind speed of the most outboard co-rotating probe. The differences originate from the fact that for the CFD codes the rotor induction cannot be separated from the undisturbed wind field. Hence, also when identical inflows are imposed, CFD codes have a lower level of the axial wind speed compared to lifting line ones, due to the rotor blockage. This is an intrinsic different between these two types of modeling, which do not allow to make a one-to-one comparison of the aerodynamics. Although this discussion is very relevant to this paper, we cannot include it in the present paper since those data are not public. However, we have included a sentence about this point in the paper.

34. *Also for this analysis I suggest removing the mean values from the plot (mentioning them in a table) and focusing only on the fluctuations (this intended for the phase-average results).*

We have tried to do that but the plot became confusing, since the lines will be mostly

superposed. Thus, we have chosen not to follow this comment.

35. *Again, if a literature results needs to be used as a comparison, it is better to show it here in order to avoid the reader going back and forth from this paper to those referenced.*

We have now included the results of Trigaux et al (2024) in figure 12.

36. *This result is expected as the lag deformation is mainly driven by gravity.*

We have now specified that.

37. *In my opinion this conclusion is quite weak if not supported by a sensitivity analysis on the number of needed modes in Elastodyn. Moreover, to me it is still unclear if the OV model really does not take into account blade torsion (see my comment on this aspect above), so, considering the absence of torsion in Elastodyn, the discrepancy could be related also to this (although this is in contrast with the lower value of lag deformation at the tip). This aspect requires more in depth investigation.*

Concerning our CFD code, as explained at page 8, the CFD-CSD/OV approach considers the torsional degree of freedom, but does not include it in the two-way coupling. Whereas, Elastodyn does not consider the torsional degree of freedom at all. Thus, we agree with the referee that this discrepancy can be related also to this point. However, we cannot extend the ElastoDyn module to consider more degrees of freedom, since it is embedded in the OpenFAST code only in this form. We have thus discussed this point in the text and stated at page 12-13 that "the four solvers employed differ in both their aerodynamic and structural modeling approaches. Moreover, the flow that impacts the turbine is not exactly the same for the CFD and OpenFAST solvers, since in the former case it is imposed at several diameters upstream the rotor plane. As a result, it is not always possible to unambiguously determine whether the observed discrepancies in the results originate from the fluid-dynamic models or from the structural formulations".

38. *Please reproduce the mentioned results in your plots!*

Done

39. *General comments to Fig 13: - the labels indicating blade eigenfrequency are hardly readable; - I suggest adding the grid lines to better appreciate the different values of the peaks. Moreover, it seems clear that blade deformation dynamics is governed by the lower components of the spectrum (the analysis of the energy content of the different harmonics should confirm this). So, although frequencies higher than the 1st flap appear, they have a very small magnitude. I suggest to reduce the x range to show only the most significant harmonics. Also the y range should be changed because as it is now it is very difficult to appreciate the peaks values. I understand that the author's aim was to show the consistency of flap/lag/torsion prediction by evidencing the role of some of the blade natural frequencies. I suggest to do this analysis only for one DOF and change the other plots using a reduced frequency range.*

We have increased the labels and added the grid lines. Also, we have increased the y axis for making the peaks more visible. The figure has an improved readability, we thank the referee for this comment.

40. *This aspect is not clear (see my previous comments on this).*

Please, see the answer to the comment number 37.

41. *This sentence is quite general and not supported by specific evidences. Aeroelasticity is a multidisciplinary topic so it must be tackled by a step-by-step approach. I agree with the choice*

presented in this work where the structural model is assessed against available literature data. What is somehow missing is its aerodynamic counterpart. Indeed, I suggest adding a purely aerodynamic comparison between the proposed CFD and other data (FAST can be an option, but ideally solvers with a similar fidelity as the one here proposed would be more appropriate). In this way the origin of the observed discrepancies can be related to the structural model, to the aerodynamic one or to their coupling.

Please, see the answer to question 33 of this referee.

42. *As the response of the system should be governed mainly by the frequencies arising from the combination of contribution stemming from aerodynamics, I suggest to comment the origin of the peaks shown in Fig 13. For instance, the rotor rotation frequency appears clearly (and it is dominant). What about the others?*

This has been done at page 23.

43. *This is not a limitation of OpenFAST but is related to the different inflow provided to the two solvers (see my comment on this above).*

We have now stated that in the text, although we specify that the CFD inflow is not turbulent, but has indeed variations in the transverse direction.

44. *Please reproduce here the cited result.*

In this particular case we have not included the cited results in the plot since the curve has many peaks and extracting it point-by-point would have induced large errors. However, we have included all the referenced results about the power coefficient and deformations, whose curves are rather simpler and more suitable to the extracted point-by-point.

45. *This is not a limitation of OpenFAST but is related to the different inflow provided to the two solvers (see my comment on this above).*

We have recalled here about the different inflow, although we do not think it is only due to the inflow conditions, which differ only slightly, but to the simplified treatment of aerodynamics.

46. *This very difficult to be seen from the plots in their current layout. Moreover, the ability of Blade Element Momentum Theory (which is inherently steady) to capture high-frequency aerodynamics is questionable. Considering the very small values of the harmonics shown around blade modes, I am not convinced that the BEM-based simulations can be so reliable.*

Here we do not refer to the high-frequency aerodynamics effects (i.e., turbulence), but to the aeroelastic (structural) high frequency vibrations. We have now better specified that.

Large Eddy Simulation of the IEA 15-MW Wind Turbine Using a Two-Way Coupled Fluid-Structure Interaction Model

Claudio Bernardi¹, Stefania Cherubini¹, Felice Manganelli¹, Giacomo Della Posta², Stefano Leonardi³, and Pietro De Palma¹

¹Department of Mechanics, Mathematics and Management, Polytechnic University of Bari, 70126, Bari, Italy (claudio.bernardi@poliba.it, stefania.cherubini@poliba.it, f.manganelli@phd.poliba.it, pietro.depalma@poliba.it)

²Department of Mechanical and Aerospace Engineering, Sapienza University of Rome, Rome, RM, 00184, Italy (giacomo.dellaposta@uniroma1.it)

³Department of Mechanical Engineering, University of Texas at Dallas, Richardson, TX, 75080, USA (stefano.leonardi@utdallas.edu)

Correspondence: Claudio Bernardi (claudio.bernardi@poliba.it)

Abstract

The aim of the work is studying the aeroelastic response of the **IEA 15 MW Reference Wind Turbine (RWT)** large-scale wind turbine using a high-fidelity fluid-structure interaction solver that combines large-eddy simulation with a modal computational structural dynamics solver through a two-way coupling. The fluid solver employs the actuator line model to simulate the interaction between the turbine blades and the fluid and the immersed boundary method to model the presence of the tower and nacelle. The results are compared with those obtained by the OpenFAST software, which is a well-known numerical tool for engineering predictions. A series of simulations have been performed with and without the presence of the tower and nacelle to better understand the effects of these components on flow structures and structural deformations. The largest discrepancies among the solvers have been observed in correspondence with the blade passage in front of the tower, which induces an abrupt alteration in the local incidence angle of the flow. Moreover, by comparing the outcomes of different structural approximations, it has been established that taking into account the torsional degree of freedom considerably affects the deformations, aerodynamic loads and power coefficient. Whereas, the nonlinearity of the solver appears to have a weak effect on the same quantities.

Keywords

Aeroelasticity, Large Eddy Simulation, Actuator Line Model, Fluid-Structure Interaction, Computational Fluid Dynamics, Computational Structural Dynamics, Blade Element Momentum, IEA-15MW Wind Turbine.

1 Introduction

Wind energy has become a crucial component of the global transition toward renewable energy sources. The increasing demand for clean energy has led to the development of large-scale wind turbines, such as the IEA 15-MW offshore wind turbine developed within IEA Wind Task 37 (Gaertner et al., 2020a). This turbine, with a rotor diameter of 240 meters and blades measuring 117 meters in length, represents a new frontier in wind energy technology (Gaertner et al., 2020b), and research is currently pointing towards even larger rotors, reaching 22-MW of power production (Zahle et al., 2024). The increasing scale and flexibility of such newly designed turbines present significant engineering challenges, particularly in predicting their aeroelastic response (Burton et al., 2011; Zheng et al., 2023). As turbines grow in size, their structural components, especially the blades, are subject to complex aerodynamic forces that cause deformations, which in turn affect the aerodynamic loads. Understanding these interactions is essential to improve the performance, reliability, and longevity of large-scale wind turbines (Manwell et al., 2010). In the worst cases, aeroelastic instabilities such as edgewise instability and flutter might even lead to blade damage, as reported for the Lunderskov Mobelfabrik 19 m wind turbine blades (Moeller, 1997), with devastating effects on the turbine performance.

[Aeroelasticity](#) is critical in the design and analysis of modern wind turbines. Aeroelastic phenomena such as dynamic stall, flutter, and [their effects on fatigue loadings](#) can have significant effects on turbine performance, particularly as the blade length increases (Hansen, 2007). These blades experience varying aerodynamic forces along their span, which can lead to substantial deformations. When blades deform, they alter the local flow field, which in turn modifies the aerodynamic loads acting on them. This feedback loop between aerodynamic forces and structural deformation makes it very difficult to predict modern large-scale turbine performance under real-world operating conditions (Vermeer et al., 2003; Wang et al., 2016a). Accurate evaluation of these interactions is key for ensuring turbine efficiency and structural integrity, especially in offshore environments where wind conditions are more severe (Bayati et al., 2017).

The numerical modeling of the blades in most of the numerical aeroelastic codes used nowadays (Schepers et al., 2021) is accomplished by the [Blade Element Momentum \(BEM\) model](#), due to its [robustness and low computational cost](#). It has been shown in the framework of the IEA WIND Task 47 Boorsma et al. (2023, 2024) that, if properly tuned, BEM can be a valuable engineering-type solver, complementary to higher fidelity ones which have also higher computational costs. However, BEM has still some limitations, since it relies on simplifying assumptions made on the impinging flow, such as [models of dynamic stall, dynamic inflow, yaw and tilt flows, and corrections of the aerofoil data for taking into account three-dimensional effects and tip losses](#). More computationally expensive models exist, such as panel methods and in general potential flow solvers and/or free-vortex wake methods, as well as the actuator disc methods. Panel and free-wake vortex methods are able to capture unsteady

blade/rotor aerodynamics with good accuracy in different operating conditions (including off-design) whenever massive flow separation phenomena do not occur Boorsma et al. (2018); Ribeiro et al. (2023). However, those models need reference high-fidelity data in order to refine and/or assess the reliability of these lower fidelity models. Therefore, the application of computational fluid dynamics (CFD) to full-scale turbines is needed as a reference for describing the complex aerodynamics of the flow field accurately (Sørensen, 2011), although for a limited number of flow case due to its high computational cost.

However, coupling three-dimensional CFD simulations with computational structural dynamics (CSD) solvers taking into account the deformation of the blade is not trivial. Three-dimensional structural finite-element models are in fact able to fully describe the complex shape of a wind turbine blade but, although accurate, these models are computationally expensive and hard to implement, leading to only a few examples of coupling with CFD codes (Bazilevs et al., 2011; Yu and Kwon, 2014). Since wind turbine blades are slender structures, their structural modeling can be more easily achieved using beam models, where the blade is discretized as a series of one-dimensional beam elements, each characterised by a given cross-sectional stiffness and mass per unit length. One-dimensional beam models can be either modal, since natural frequencies and mode shapes of a turbine are directly related to the natural frequencies of its blades, or they can rely on the geometrically exact beam theory including non-linear effects (Sabale and Gopal, 2019).

Due to their ability to provide a rapid evaluation of the turbine performance, numerical tools based on the BEM approach equipped with aeroelastic modules based on one-dimensional beam models, are currently widespread (Schepers et al., 2021). A notable example is OpenFAST, a numerical code developed at NREL (Jonkman, 2013) and widely used for aeroelastic simulations, which employs BEM theory for aerodynamic modeling and various structural solvers, such as ElastoDyn (Damiani et al., 2015) and BeamDyn (Wang et al., 2016b), for structural deformation analysis. However, it is still not clear whether the predictions of such lifting-line aeroelastic codes are sufficiently accurate for large-scale turbines, in which the effect of shear and inflow turbulence can lead to complex inflows and turbine aerodynamic responses. Comparing the predictions of OpenFAST with those of a Large-Eddy Simulation (LES) equipped with a structural one-dimensional beam model has shown that, for an NREL 5MW wind turbine, the passage in front of the tower leads to large deformations which are largely underestimated by OpenFAST (Bernardi et al., 2023).

Concerning rotors of even larger size, such as the IEA 15-MW reference turbine, it is not yet known whether these discrepancies in the predictions of lifting-line codes with respect to CFD are even more consistent. Using the unsteady Reynolds-Averaged Navier-Stokes (URANS) equations coupled with an aeroelastic module, as reported by Pagamonci et al. (2023), has shown that neglecting the flexibility of the blades in numerical simulations leads to an underestimation of the rotor thrust of approximately 2.5% for the IEA 15-MW turbine, which is not observed for the smaller NREL 5MW rotor. Moreover, this work also concluded that the deformation of long, slender blades may act as a filter for the high-frequency fluctuations arising from the flow field, proving that taking into account the blades' aeroelasticity in the design process of these machines is key for the future upscaling of turbine rotors. Furthermore, Trigaux et al. (2024) observed how the use of high-fidelity aerodynamic models is crucial to predict the aeroelastic effects of large rotors. These results suggest the need to investigate this issue resorting to LES, which is capable of describing the dynamics of the flow more accurately.

In this context, the present work aims at studying the aeroelastic response of a large-scale 15-MW wind turbine by means of LES, assessing the effect of the flexibility of the blades on the wake dynamics. The results are compared with those obtained by more simple and less computationally expensive models, such as the OpenFAST code. Computations are performed by an in-house LES code using the immersed boundary method to model the tower and nacelle and the Actuator Line Model (ALM) for blade modeling, coupled with a structural modal solver, originally developed by Della Posta et al. (2022).

The discussion of the results highlights the role of the tower and nacelle in the dynamics of the aerodynamical forces, thrust and power coefficients, as well as in the distribution of turbulent kinetic energy within the wake, which could have an impact on the aerodynamic loads of downstream turbines in wind farms. Moreover, the effect of the torsional degree of freedom has been investigated by comparing the outcomes of different structural approximations.

The work is structured as follows. In section 2, the aerodynamic and structural solvers of both CFD-CSD and OpenFAST codes are described in detail. In section 3, the numerical setup is presented. In section 4, relevant results are discussed, and conclusions are drawn in section 5.

2 Methodologies

2.1 CFD-CSD solver

2.1.1 Flow solver

The simulations of the flow around the wind turbine are carried out through Large-Eddy Simulations (LESs) of the incompressible, filtered, 3D Navier-Stokes equations, employing the in-house UTD-WF solver introduced by Santoni et al. (2015). The UTD-WF framework has been progressively developed by Santoni et al. (2017, 2020) and further extended by Della Posta et al. (2022, 2023), where the aeroelastic solver and the Leishman–Beddoes dynamic stall model were implemented. The solver has been validated in its non-aeroelastic version by Santoni et al. (2017) against wind-tunnel data reproducing the NTNU “Blind Test” and comparing simulations to Krogstad et al. (2015) measurements, also considering the impact of tower and nacelle. Whereas, the recently developed version of the code including the two-way FSI coupling Della Posta et al. (2023) has been validated through comparison against reference datasets, including HAWC2-based results reported by Heinz (2013). The IEA 15MW wind turbine configuration considered here has been cross-validated with many other aeroelastic numerical codes in the International Energy Agency (IEA) Wind TCP Task 47 (Cacciola et al., 2025), also considering turbulent inflow conditions (Schepers et al., 2025). Notice that prior validations by Della Posta et al. (2022) of the CFD-CSD solver were made on a laminar uniform and a turbulent sheared inflows for a 5 MW NREL turbine, whereas our study extends the validated setting to the IEA-15 MW case for a sheared laminar inflow configuration. However, as discussed in the framework of the IEA Wind TCP Task 47 Schepers et al. (2025), turbulent fluctuations appear to have a much stronger impact than shear on load response of aero-elastic numerical codes. Moreover, high-fidelity codes appear rather consistent in predicting loads, while engineering models tend to overpredict fatigue loads, particularly for large rotors (Cacciola et al., 2025).

The code implements a second-order accurate centered finite difference scheme for the spatial dis-

cretization on a staggered Cartesian grid. A hybrid low-storage third-order-accurate Runge–Kutta (RK) scheme is used for time integration of the non-linear terms (Orlandi, 2012), while the linear terms are treated implicitly using a Crank-Nicolson scheme. The filtered governing equations are:

$$\frac{\partial u_i}{\partial t} + \frac{\partial u_i u_j}{\partial x_j} = -\frac{\partial p}{\partial x_i} + \frac{1}{Re} \frac{\partial^2 u_i}{\partial x_j \partial x_j} - \frac{\partial \tau_{ij}}{\partial x_j} + \tilde{f}_i, \quad (1)$$

$$\frac{\partial u_i}{\partial x_i} = 0, \quad (2)$$

where $i, j \in \{1, 2, 3\}$ represent, in a Cartesian reference frame, the components along the streamwise (x), wall-normal (y), and spanwise (z) directions, respectively. The Reynolds number $Re = U_\infty D / \nu$ is defined by the undisturbed inlet velocity U_∞ , the turbine diameter D , and the kinematic viscosity of the fluid ν . These quantities are used as reference values to make the equations non-dimensional. To solve the filtered equations, a Subgrid-Scale (SGS) stress model is needed. The latter describes the interaction between the large resolved and the sub-grid unresolved scales, as described by Pino Martín et al. (2000) and Santoni et al. (2017). Here, we employ the Smagorinsky model with constant $C_s = 0.09$ as discussed by Martinez-Tossas et al. (2018).

The effect of the blades on the flow is modeled by the Actuator Line Model (ALM) (Sørensen and Shen, 2002), by adding a forcing term to the Navier-Stokes equations, representing the force per unit volume exerted by the rotor on the fluid. By approximating the rotor blades as straight lines discretized into segments, it is possible to estimate the lift and drag forces per unit length on a 2D plane as follows:

$$F_l = \frac{1}{2} \rho u_{rel}^2 C_l(\alpha) c F, \quad F_d = \frac{1}{2} \rho u_{rel}^2 C_d(\alpha) c F, \quad (3)$$

where ρ is the air density, c is the local chord, u_{rel} is the relative incoming velocity, α is the angle of attack, and F represents the tip loss correction factor, which employs the tip-loss model proposed by Shen et al. (2005). The coefficients c_1 and c_2 of this model have been set in the following way: c_1 has been set to the value reported in the Shen et al. (2005) paper ($c_1 = 0.125$), whereas, c_2 has been chosen after a calibration with respect to the forces close to the tip reported by OpenFAST for the same turbine and flow case, leading to the choice of $c_2 = 32$. The forces are then projected on the flow employing a 2D Gaussian kernel, which spreads the lift and drag force vector, \mathbf{f}^{aero} , in cylinders surrounding the actuator line,

$$\tilde{\mathbf{f}} = -\mathbf{f}^{aero} \frac{1}{\epsilon^2 \pi} \exp \left[-\left(\frac{r_\eta}{\epsilon} \right)^2 \right], \quad (4)$$

where r_η is the radial distance of a generic point of the cylinder from the actuator line and ϵ is the spreading parameter, where $\epsilon / \Delta \geq 2$, with $\Delta = \sqrt{\Delta x^2 + \Delta y^2 + \Delta z^2}$, following Troldborg (2009). The tower and nacelle are modeled using the Immersed Boundary Method (IBM) following the approach described by Orlandi and Leonardi (2006).

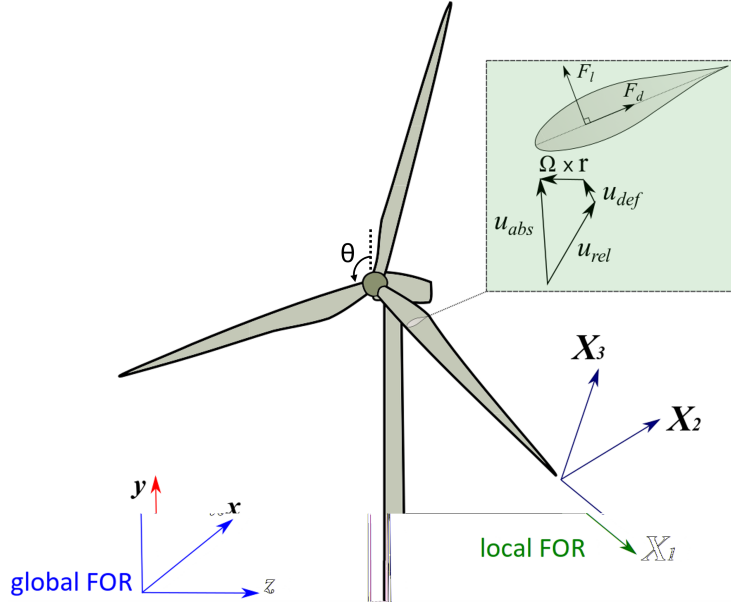


Figure 1: Sketch of the frames of reference used for the CFD and for the CSD simulations.

2.1.2 Structural solver

From an aerodynamic standpoint, the rotor blades represent the most flexible components within a wind turbine. Several studies demonstrated that their modal properties have a significant impact on the dynamics of the entire structure (Damgaard et al., 2013; Dong et al., 2018). Moreover, an analysis of the isolated blades is also sufficient to accurately estimate the aeroelastic properties of the entire structure, including the flutter speed (Abdel Hafeez and El-Badawy, 2018). Additionally, the tower and shaft exhibit minimal deflection due to their stiffness. In light of the above considerations, the aeroelastic model is constructed to encompass solely the structure of the blades.

The structural model used in the present study was extensively described by Della Posta et al. (2022, 2023) and will only be briefly outlined here. Under the assumption of small deformations with respect to a relative frame of reference (FOR), the blades are assumed to be rotating beams rigidly clamped at the hub (cantilever beams). Moreover, it is assumed that the blade deformation does not modify the rotor inertia. With these hypothesis, a linear structural dynamic equation is obtained, taking into account the Coriolis, centrifugal and Euler effects, that will be given in the following. Let us denote by X_1 the direction of the pitching axis. This coincides with the neutral axis of the blade, defined as passing through the quarter of the chord. The direction of the out-of-plane flapwise motion is indicated by X_2 and is oriented in the positive streamwise direction. The in-plane edgewise direction of X_3 is defined such that the FOR is oriented as a right-handed coordinate system (Figure 1).

Under the assumption of linearity, the elastic generalised displacement $\mathbf{d} = (d_i, \theta_i)$, which includes translational d_i and rotational θ_i (with $i = \{1, 2, 3\}$) degrees of freedom (DoFs), is decomposed along the coordinate X_1 on the neutral axis as:

$$\mathbf{d}(X_1, t) = \sum_{m=1}^M q_m(t) \psi^m(X_1), \quad (5)$$

where $\psi^m(X_1)$ is the m -th elastic mode shape from the modal analysis of the structure, q_m is the corresponding modal coordinate, and M is the number of modes used. The effect of the generic motion of the FOR on the relative structural dynamics (one-way inertial coupling, since we assumed that the blade deformation does not modify the rotor inertia) is included in a modal basis by means of the methodology introduced in Reschke (2005) and further developed for the case of wind energy in Della Posta et al. (2022). Through this method, which exploits the decomposition of the acceleration in a moving FOR in the virtual work principle, we obtained a system of elastic equations with additional stiffening, damping, and loading terms depending on the angular velocity and acceleration of the rotating FOR, as:

$$\mathbf{M}\ddot{\mathbf{q}} + [\mathbf{D} + \mathbf{D}^{Co}(\Omega)]\dot{\mathbf{q}} + [\mathbf{K} + \mathbf{K}^c(\Omega) + \mathbf{K}^{Eu}(\dot{\Omega})]\mathbf{q} = \mathbf{e} + \mathbf{e}^c(\Omega) + \mathbf{e}^{Eu}(\dot{\Omega}), \quad (6)$$

where \mathbf{M} , \mathbf{D} and \mathbf{K} denote the modal structural mass, damping, and stiffness matrices, respectively, and \mathbf{e} are the external loads expressed in modal basis, including the gravity force acting on the local centre of mass and the ALM aerodynamic forces acting on the local quarter of chord. The remaining terms are inherently related to the various contributions to the acceleration in a moving FOR. Terms with the superscript Co , c and Eu are related to the Coriolis, centrifugal, and Euler accelerations, respectively. Given the assumption of linearity, we apply all the forces to the reference undeformed configuration. The discrete evaluation of the additional inertial terms in Equation (6) is expressed as a function only of the information known from the structural finite-element method (FEM) model and from the corresponding mode shapes, according to Saltari et al. (2017). For the modal analysis, performed on the undeformed nonrotating blade, we use a finite element model of the blade based on complete beam elements with 6 DoFs, with Euler-Bernoulli behavior for bending in directions X_2 and X_3 , and linear shape functions for axial and torsional deformations. We assume a lumped-mass representation, and we take into account the local offset of the centers of mass with respect to X_1 . Finally, the structural matrices are assembled considering the local twist. The generalized- α method (Chung and Hulbert, 1993) is employed to advance the structural dynamic equation in time, which is unconditionally stable for linear problems, and second-order accurate. Details about the modal analysis are provided in Appendix A.

2.1.3 Fluid-structure interaction model

The two-way coupling aeroelastic model employs the ALM sectional approach, whereby the angle of attack (AoA) and relative velocity are locally modified following the instantaneous blade motion provided by the structural dynamics. In particular, the distribution of the AoA along each blade is evaluated as a function of the velocity of the fluid, the angular velocity of the rotor, and the instantaneous elastic state of the blade (which is projected back to the physical space from the modal one once the displacement is determined). The latter is generally constructed from the deformation velocity $\mathbf{u}_{def} = \dot{\mathbf{d}}_{tr}$, considering the time derivative of the translational degrees of freedom only, and the local vector of the deformation angles $\boldsymbol{\theta}$ (torsion, and in-/out-of-plane angular deformations)

derived from the structural solver, which is forced by the updated aerodynamic loads. The algorithm restricts inter-field communications solely at the beginning of each RK substep, thereby ensuring optimal computational efficiency. The impact of the torsional dynamics was deemed to be limited in light of the results obtained in previous studies on the effect of torsion for smaller wind turbines (Chen, 2017). In order to investigate this issue for the large rotor 15MW wind turbine, in this study we compare two different CSD models. In particular, we consider as a baseline a two-way coupling that includes the effect of blade deformation velocity as a sole variable (CFD-CSD/OV, for Only Velocity), and a more complete model including the torsional deformation in the coupling (CFD-CSD/T, for Torsional). In general, the relative velocity for a rotating blade can be defined with the following expression:

$$\mathbf{u}_{rel} = \mathbf{u}_{abs} - \boldsymbol{\Omega} \times \mathbf{r}_{OP} - \mathbf{u}_{def}, \quad (7)$$

where \mathbf{u}_{abs} is the filtered velocity from the fluid solver at the actuator line, \mathbf{r}_{OP} is the general radial vector pointing to the considered section, Ω is the rotor rotational speed, and \mathbf{u}_{def} is the deformation velocity of the structure at the same position. As a result, the AoA used to determine the air load coefficients is defined as follows:

$$\alpha = \text{atan} \left(\frac{\mathbf{u}_{rel} \cdot \mathbf{E}_2}{-\mathbf{u}_{rel} \cdot \mathbf{E}_3} \right) - \phi - \theta_{tors} = \text{atan} \left[\frac{(\mathbf{u}_{abs} - \mathbf{u}_{def}) \cdot \mathbf{E}_2}{\Omega r - (\mathbf{u}_{abs} - \mathbf{u}_{def}) \cdot \mathbf{E}_3} \right] - \phi - \theta_{tors}, \quad (8)$$

where ϕ is the local twist angle of the blade, θ_{tors} is the local torsional deformation, \mathbf{E}_i are the unit vectors of the relative FOR rotating with the structure, and hence, $v_2 = \mathbf{u}_{def} \cdot \mathbf{E}_2$ is the flapwise deformation velocity component, and $v_3 = \mathbf{u}_{def} \cdot \mathbf{E}_3$ is the edgewise deformation velocity component. The simplified coupling procedure benefits from the sectional one-dimensional formulation of the ALM, which avoids the complex treatment of the fluid-solid interface with the associated kinematic and traction conditions.

3 Flow and structural setup

In this work, we consider a stand-alone IEA 15-MW wind turbine (Gaertner et al., 2020b) in its monopile configuration. This wind turbine has a rotor diameter $D = 240$ m with three blades of length $L = 117$ m. Table 1 provides the main features of the turbine.

The computational domain has dimensions $12.5 \times 5 \times 3$ diameter units, as shown in Figure 2. The distance of the turbine from the inlet of the computational domain (equal to 4D) has been determined on the base of the reference data available in the literature, which vary in the range 2D-5D. Smaller distances from the inlet (2D) have been employed for experimental set-up (Bartl and Satran, 2017; Krogstad et al., 2015), whereas larger distances (in the range 2.7D-5D) are typical of numerical simulations (Porte-Agel and Wu, 2011; Ciri et al., 2017; Allah and Sha ei Mayam, 2017; Stevens et al., 2018). Moreover, we have verified numerically that pressure fluctuations do not generate spurious reflections at the inlet section in our simulations. The spanwise length of the computational domain (equal to 3D) is the same employed in previous numerical simulations (Ciri et al., 2017; Allah and Sha ei Mayam, 2017). We have verified that, using periodic boundary conditions, the blockage effect

on the single turbine is negligible. Moreover, following the convergence study reported in the Appendix A, the computational box has been discretized by a staggered grid composed of $2049 \times 513 \times 513$ points in the streamwise, wall-normal, and spanwise directions, respectively. The orthogonal grid is equally spaced in the streamwise and spanwise directions and is stretched vertically, with a gradually wider spacing starting from the region above the rotor. The grid spacing described leads to an actuator line discretized by 86 points per blade. The time resolution of the LES computation is tied to the spatial resolution, as defined by the stability requirements of the numerical scheme adopted. Simulations are carried out at a constant Courant–Friedrichs–Lewy (CFL) number (Courant et al., 1967) $CFL = 0.65$, which ensures an average time step $\overline{\Delta t} = 0.024s$. The turbine location is 4 diameter units from the inlet and centered in the spanwise direction. Furthermore, we impose a sheared laminar inflow velocity profile, defined by a power law with the exponent $\alpha = 0.05$, and a convective outlet boundary condition, i.e., $\frac{\partial u_i}{\partial t} + C \frac{\partial u_i}{\partial x} = 0$, with the constant C set to the average value of the outflow velocity. Notice that, as the shear is imposed at the inlet, the flow profile is allowed to change when reaching the turbine. However, since the power law profile complies with the no-slip conditions at the wall and with the slip conditions at the free-stream, the modifications are mostly due to the slight three-dimensionalization of the flow due to the presence of the turbine. In the spanwise direction, periodic boundary conditions are imposed. Moreover, slip and no-slip conditions are enforced at the top and bottom boundaries, respectively. The turbine is subjected to a flow with a Reynolds number $Re \approx 10^8$ and operates at its nominal tip speed ratio (TSR) of $\lambda = 9$. The streamwise undisturbed velocity at the hub height is constant and equal to $U_\infty = 10 \text{ m/s}$. The simulations were conducted for a time interval of 300 s over the initial transient, which corresponds to 35 revolutions of the rotor.

To identify the optimal configuration for the structural model, we conducted a preliminary sensitivity analysis and then validated the structural eigenfrequencies of the undeformed nonrotating blade with the results found in the literature. A more detailed insight into this analysis is presented in Appendix B, where the structural properties of this turbine are shown. Finally, a number of modes $M_s = 15$ and a structural discretization of the blades given by $N = 80$ equally-spaced nodes were chosen. For comparison purposes, wind turbine simulations have been also conducted using the OpenFAST solver *Release v3.2.0* (July 29, 2022). The aerodynamic computations are performed by the *AeroDyn* (Jonkman et al., 2015) module which is based on the BEM theory. A Prandtl loss model is applied to account for the tip and root effects. The structural module dedicated to the computation of the blade deformation is contained in the *BeamDyn* module, which relies on the geometrically exact beam theory and may resolve geometric non-linearities and large deflections (Wang et al., 2016b). In order to compare the CFD-CSD results with a modal structural analysis, we also performed simulations using the standalone *ElastoDyn* module, based on a modal approach and suitable for blade deformation dominated by bending. It is worth to notice that the latter does not take into account the torsional degree of freedom, so it is to be directly compared to the CFD-CSD/OV model, which also does not account for the coupling between the torsional deformation and the angle of attack. As reported in the original manual of *AeroDyn* (Moriarty and Hansen, 2005), OpenFAST couples the fluid and structural solvers in a similar way to our CFD-CSD solvers. In particular, the local angle of attack is determined taking into account the local deformation velocities.

| Parameter | Units | Value |
|--------------------------|-------|--------|
| Power rating | MW | 15 |
| Rotor diameter (D) | m | 240 |
| Rotor orientation | — | Upwind |
| Number of blades | — | 3 |
| Blade length (L) | m | 117 |
| Hub height | m | 150 |
| Hub radius (R_{hub}) | m | 3.97 |
| Rated wind speed | m/s | 10.59 |
| Design tip speed ratio | — | 9 |
| Maximum rotor speed | RPM | 7.56 |

Table 1: IEA 15-MW (Gaertner et al., 2020b) wind turbine main features

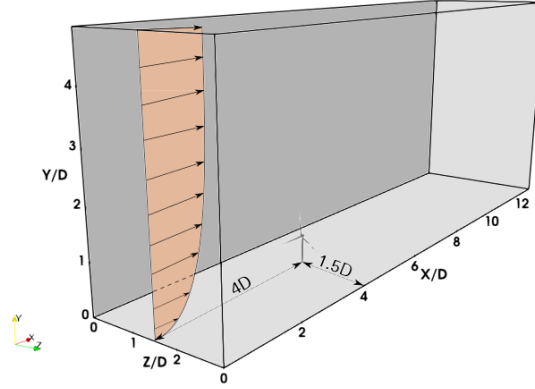


Figure 2: Sketch of the computational domain where the incoming sheared flow and the position of the turbine are highlighted.

4 Results and discussion

This section presents the results of two set of simulations: one modeling a rotor-only configuration (RO) and the other including the tower and nacelle (TN). Furthermore, both configurations are subjected to comparative analysis using the OpenFAST submodules. Firstly, the near-wake aerodynamic characteristics and the wake recovery of both configurations determined by the CFD-CSD solvers are discussed. Then, the aerodynamic loads on the blades are analyzed and the outcomes from both solvers are compared. Finally, the overall turbine performance and the effects on the blade deformation are assessed.

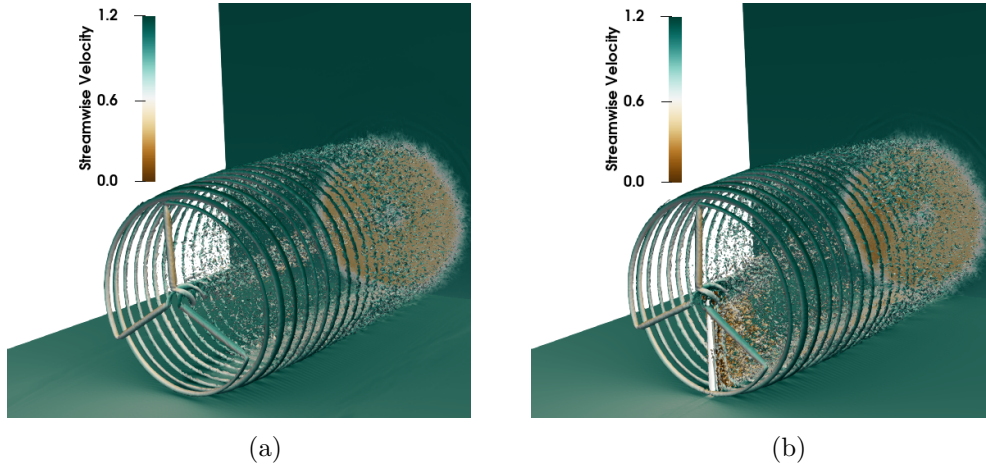


Figure 3: Q-criterion contour of the instantaneous velocity field colored by the streamwise velocity for the rotor-only case (RO) (a) and tower and nacelle (TN) (b).

4.1 Flow analysis

As a first step, we analyze the flow field variables, as obtained using the CFD-CSD/T solver. Figure 3 illustrates the main coherent flow structures in the field by means of an instantaneous isosurface of the Q-criterion colored by the streamwise velocity for both cases. It is evident that the presence of the tower affects the vorticity intensity distribution along the vertical direction. In particular, the occurrence of a low-velocity recirculation zone at the tower height for the TN case can be identified, which is a result of the tower shadowing (see Figure 3b). Moreover, the TN case demonstrates a more rapid dissolution of the endogenous coherent hub vortex structures if compared to the RO case (see Figure 3a). On the other hand, the tip vortex structures appear to be minimally influenced by the presence of the tower. Figure 4 shows the rotor-averaged streamwise velocity along the flow direction, time-averaged over 30 revolutions of the rotor. Contrary to what Santoni et al. (2017) observed in their work on the 5MW reference turbine invested by a uniform inflow (see the red lines in figure 4), the rotor-averaged velocity for the TN configuration in the wake remains slightly lower than for the OR case, indicating that wake recovery is slightly hindered by the presence of the tower. Although further validation is required as the result does not fully align with this previous literature study, wake recovery appears thus to be hindered by tower presence. One possible explanation for this behaviour could be differences in the tower-to-rotor aspect ratio. In particular, for the NREL 5-MW turbine, the ratio between the tower diameter and the rotor diameter is about equal to 0.047, whereas, for the 15MW turbine, it is only about 0.027 (the tower diameters being 6m and 6.5m, respectively). Thus, the thinner shape (in terms of diameter units) of the tower, as well as the lower value of the incoming velocity at the tower height due to the presence of shear at the inflow, result into a decreased mixing behind the turbine which leads to a slower wake recovery.

From an energy perspective, the wake recovery process can be depicted by examining the Turbulent Kinetic Energy (TKE) in the wake. Figure 5 represents the time-averaged TKE for both configurations on different planes. The TN case exhibits high TKE values in the near wake, in the region just

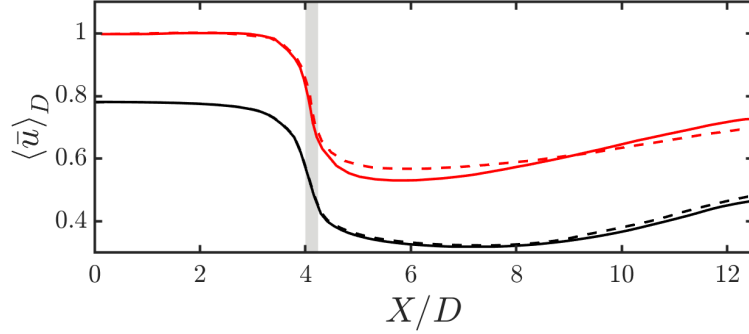


Figure 4: Rotor-averaged velocity along the streamwise direction normalized by the undisturbed velocity at the rotor height, namely, $U_\infty = 10 \text{ m/s}$, for the present data (black curves) and the work of Santoni et al. (2017) (red curves). The grey region represents the area covered by the rotor. (RO ----, TN —).

downstream of the tower and nacelle. The top view of the TN case shows that the TKE in the wake presents an asymmetric distribution as De Cillis et al. (2022) observed, among the others, in their work. On the contrary, the RO configuration shows large TKE only in the far wake region, with large values also in the region above hub height. **This result may indicate** that the tower does not increase the kinetic energy entrainment but it rather has a slight shielding effect on wake recovery. Although not favoring kinetic energy entrainment, the tower still plays a strong role in the wake dynamics, as it can be visualized in Figure 6, showing slices of instantaneous streamwise velocity at different tower heights corresponding to 80% of the blade (top) and to the tip of the blade (bottom), when the blade is in front of the tower, i.e. $\theta = 180^\circ$ (left), and when it is far from it (right). In particular, it can be observed that the turbulent mixing right downstream of the tower is already very high in the near wake compared to that close to the tip of the blades. **Due to the mutual effect of the asymmetry induced by the rotation of the blades and of the wake meandering, it can be seen that, inside the rotor disk, the tower wake bends in the spanwise direction (Figure 6, top frames),** whereas it is rather spanwise independent at a height corresponding to the blade's tip (bottom frames). Moreover, one can see that the passage of the blade in front of the tower (left frames) induces a strong perturbation in the flow field already upstream of the tower. In the following section, the effect of this perturbation on the phase oscillations of several relevant quantities (aerodynamic forces, power coefficient, etc.) will be discussed.

4.2 Aerodynamic loads on the blade

The analysis of the aerodynamic loads on the blade has been conducted using the present CFD-CSD models and the engineering software OpenFAST. The same laminar sheared inflow is imposed for both solvers using a power law with the same exponent and reference streamwise velocity at the hub height. We have chosen not to impose a turbulent inflow to avoid differences in the definition of the turbulent inflow itself which might have hindered the comparison between the results of the two codes. **It is important to note that the four solvers employed differ in both their aerodynamic and structural**

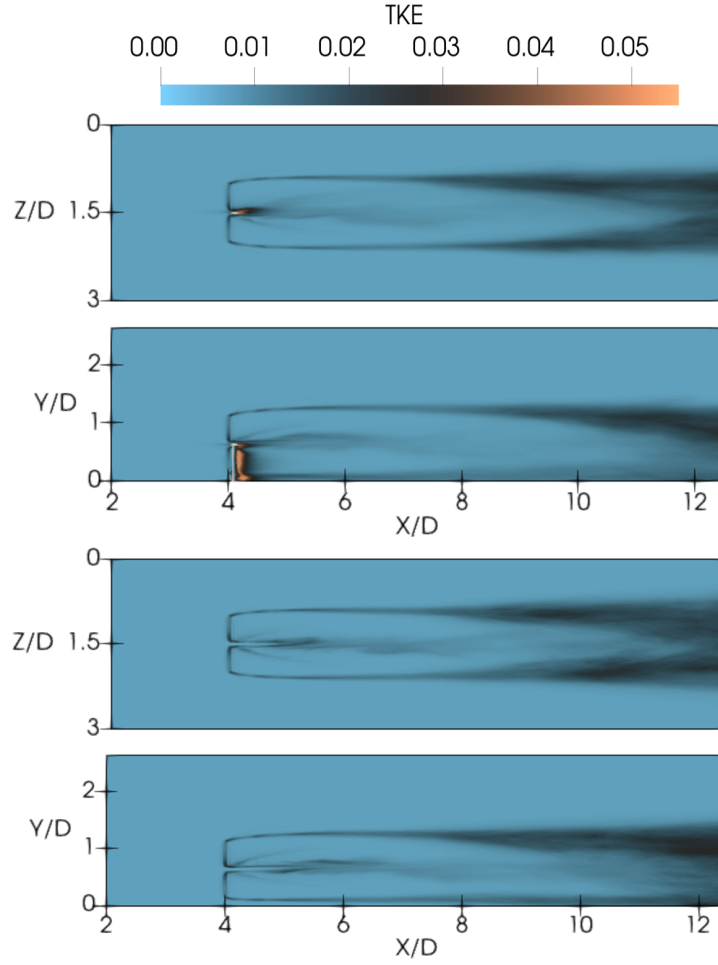


Figure 5: Top (first and third slice) and lateral (second and fourth slice) views of the time-averaged Turbulent Kinetic Energy on slices passing through the hub. TN (first and second slice), RO (third and fourth slice).

modeling approaches. Moreover, the flow that impacts the turbine is not exactly the same for the CFD and OpenFAST solvers, since in the former case it is imposed at several diameters upstream the rotor plane. As a result, it is not always possible to unambiguously determine whether the observed discrepancies in the results originate from the fluid-dynamic models or from the structural formulations.

Figure 7 depicts the following time-averaged aerodynamic quantities along the span of the blade: the local angle of attack α (Figure 7a); the aerodynamic pitching moment per unit length M_{aero} (Figure 7b); the flapwise and edgewise components (normal and tangential to the rotor disk, respectively) of the aerodynamic force per unit length F_2 (Figure 7c) and F_3 (Figure 7d), respectively. In particular,

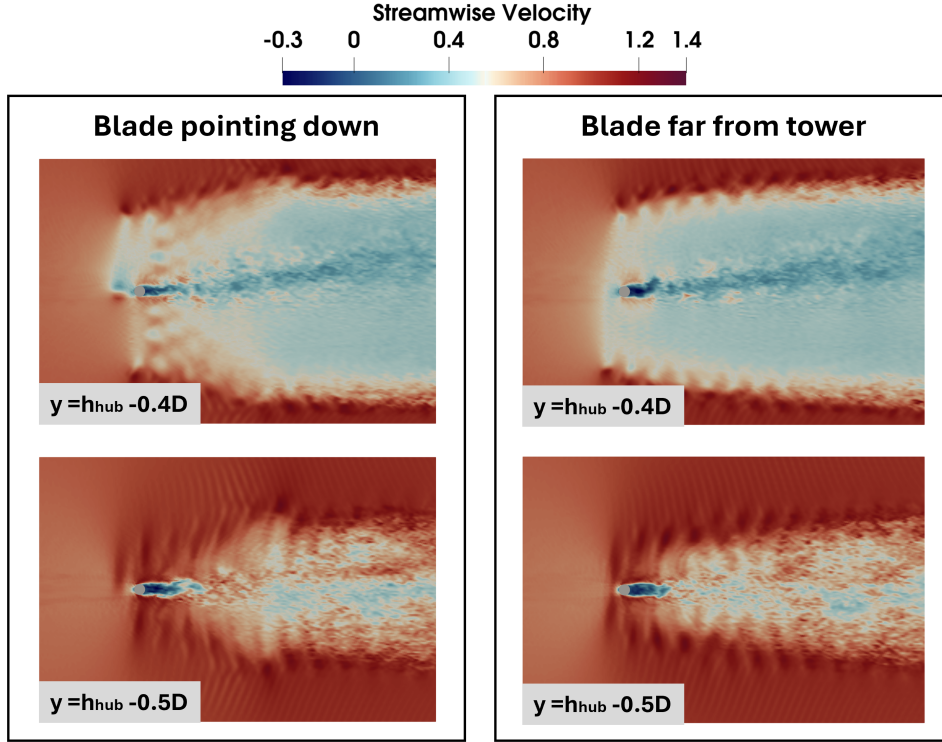


Figure 6: Instantaneous streamwise velocity on horizontal slices at different tower heights corresponding to 80% of the blade (top slices), and the tip of the blade (bottom slices). In the left configuration, the blade is in front of the tower ($\theta = 180^\circ$), while on the right the blade is far from the tower. $h_{hub} = 0.625D$ is the hub height.

Figure 7a shows that a good agreement of the local incidence angle computed by both CFD-CSD models (solid lines) with that computed by *ElastoDyn* (circles) and *BeamDyn* (squares) is obtained from the 20% up to the 80% of the blade length. Indeed, the differences in the root area could be ascribable to the presence of the hub which is modeled differently by the solvers. The discrepancy of the incidence angle observed towards the tip subsequently affects the aerodynamic loads. The F_2 force in Figure 7c shows a very good fit of the CFD-CSD/T results with that of the nonlinear solver *BeamDyn*, despite the linearity of our in-house CSD model. The strong discrepancies with respect to the values obtained by *ElastoDyn* can be ascribed to the absence of the torsional deformation in the latter solver. Indeed, the CFD-CSD/OV solver, which neglects the torsional feedback in the coupling, shows very similar results to the *ElastoDyn* solver. A similar effect can be observed by examining the reduction in F_3 towards the tip of the blade (see Figure 7d). The distribution of the aerodynamic pitching moment presents instead a maximum gap of about 8% from the BEM-based solvers. As demonstrated by Hansen (2015), the outer third of the blade span is the most critical region in terms of deflections and deformations due to the combination of higher aerodynamic loads and reduced structural stiffness. Therefore, a phase average of the aerodynamic quantities at the 80% of the blade

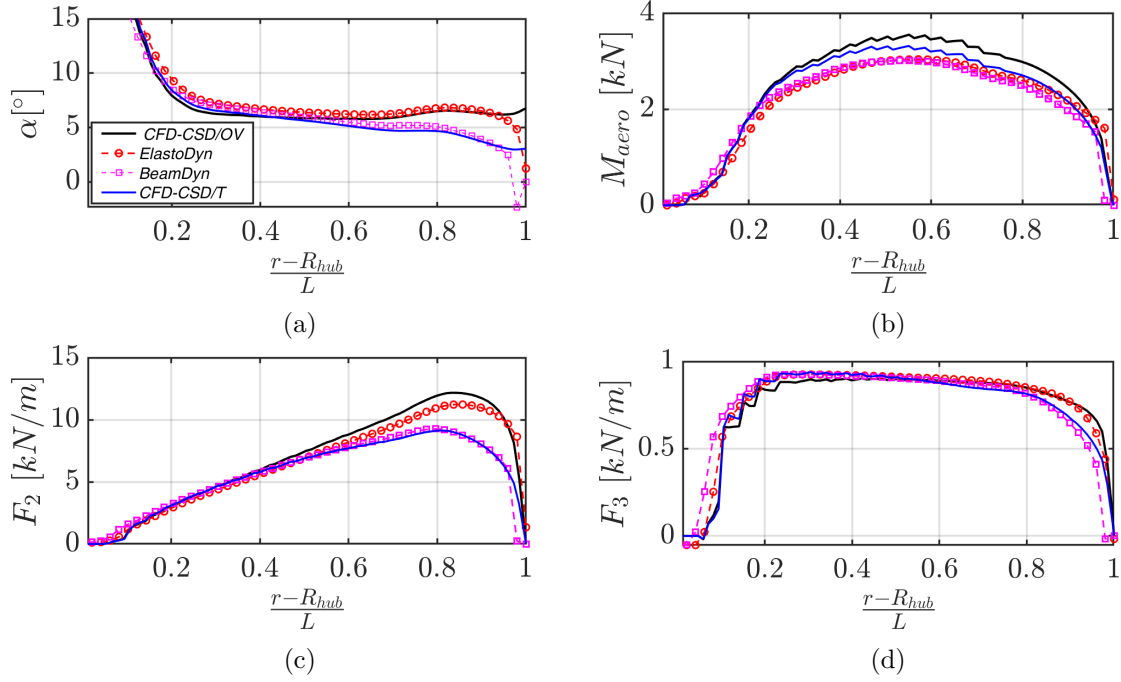


Figure 7: Average aerodynamic quantities along the blade compared between CFD-CSD/OV, CFD-CSD/T, *ElastoDyn*, and *BeamDyn*. (a) Incidence angle, (b) Aerodynamic pitch moment, (c) flapwise aerodynamic force, (d) edgewise aerodynamic force.

has been performed. Figure 8 reports the evolution of the incidence angle and of the aerodynamic force components at $\frac{r-R_{hub}}{L} = 0.8$ (being R_{hub} the hub radius and L the blade length) versus the blade rotation angle θ . The dynamical behavior of the aerodynamic quantities in the presence (solid lines) or in the absence (dashed lines) of the tower underlines that the passage of the blade in front of the tower represents the main source of instability for the flow conditions considered. Indeed, the blade-tower interaction **leads to oscillations** of the aerodynamic forces and of the incidence angle around $\theta = 180^\circ$, i.e., when the blade is pointing down. However, unlike the case of the NREL 5-MW turbine (Bernardi et al., 2023), this effect appears to be stronger for the BEM computations than for the CFD-CSD solver. Concerning this point, we should recall that, as pointed out by Bernardi et al. (2023), the complex flow dynamics resulting from the interaction between the blade and the tower, shown in Figure 6, may not be well described by OpenFAST, which uses a simple potential flow model. It can be observed that, between the rotor and the tower, a region with low streamwise velocity is observed. We can expect that the passage of the blade in front of the tower thus induces an alteration of the aerodynamic forces on the blade due to the decrease/increase of the streamwise velocity. This issue will be further discussed in the following, where a possible reason for the different behavior observed for the IEA 15-MW with respect to the NREL 5-MW turbine will be discussed.

Apart from the effect of the tower, one can observe a rather good match between the CFD-CSD/OV and *ElastoDyn* solvers for both the incidence angle and the edgewise component of the aerodynamic

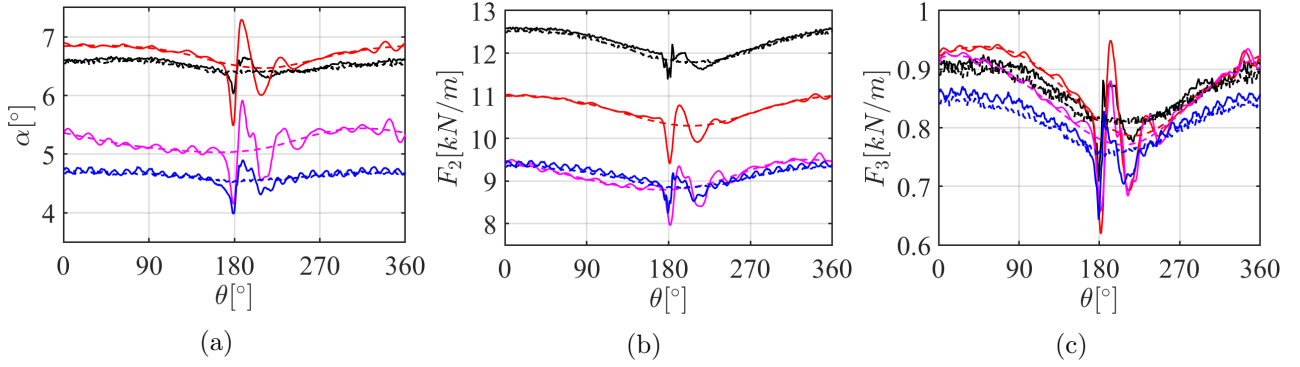


Figure 8: Phase-averaged values of: (a) the local incidence angle, (b) flapwise aerodynamic force, and (c) **edgewise** aerodynamic force at the 80% of the blade. CFD-CSD/OV: TN —, RO ----. CFD-CSD/T: TN —, RO ----. *ElastoDyn*: TN —, RO ----. *BeamDyn*: TN —, RO ----.

force, while the flapwise component presents some discrepancies. On the other hand, when torsional feedback is included, CFD-CSD/T and *BeamDyn* solvers, **regardless of the linearity or non-linearity of the models, agree rather well on the aerodynamic forces, especially on the flapwise one, which shows an error $\approx 2\%$, while the edgewise force reaches a $\approx 5\%$ error at azimuthal angles close to $\theta = 0$. Whereas, the error between the two solvers on the angle of attack reaches 8%.**

To better investigate the local response of the different models during the blade revolution, we conducted a comparative analysis of the aerodynamic loads, employing phase-averaged quantities over the span. Figure 9 illustrates the percentage difference of the phase-averaged aerodynamic quantities on the rotor plane of the *ElastoDyn* (*BeamDyn*) solver with respect to the CFD-CSD/OV, defined as $|\langle \Delta\alpha/\alpha^{CFD-CSD/OV} \rangle\%|$, and of the CFD-CSD/T model, defined as $|\langle \Delta\alpha/\alpha^{CFD-CSD/T} \rangle\%|$, respectively. In particular, in comparison to *ElastoDyn*, a higher value of the absolute incidence angle in the range of $|\langle \Delta\alpha/\alpha^{CFD-CSD/OV} \rangle\%| = [17\%, 25\%]$ is found in the zone after the tower (see Figure 9a). The difference with respect to the results obtained by *BeamDyn* tends to be higher moving from the root to the tip with a discontinuity in the tower area, spanning the range $|\langle \Delta\alpha/\alpha^{CFD} \rangle\%| = [35\%, 60\%]$ in the last 20% of the blade span. Furthermore, the angle of attack distribution affects the components of the aerodynamic force. In fact, the distribution of the flapwise component of the force follows the same pattern of the incidence angle (see Figure 9b). On the other hand, for the edgewise component the major discrepancies are concentrated in the final radial sections of the blade toward the tip (see Figure 9c). In general, we can conclude that the most significant discrepancies are observed in the tip region where the three-dimensional effects are more relevant and where the complexity of the fluid flow is strongly affected by the presence of the tower.

Notably, similar discrepancies are observed when comparing the CFD-CSD/T solver with the *BeamDyn* solvers. However, in this case some high-frequency oscillations are observed for the three aerodynamic quantities. In fact, the same oscillations are observed in the phase averaged quantities at 80% of the blade shown in Figure 9, for both the CFD-CSD/T solver and *BeamDyn*. The frequency of these oscillations **computed by the two solvers appear very close** and comparable with the natural frequency of the first torsional mode, **although some differences can be observed in the amplitudes of the**

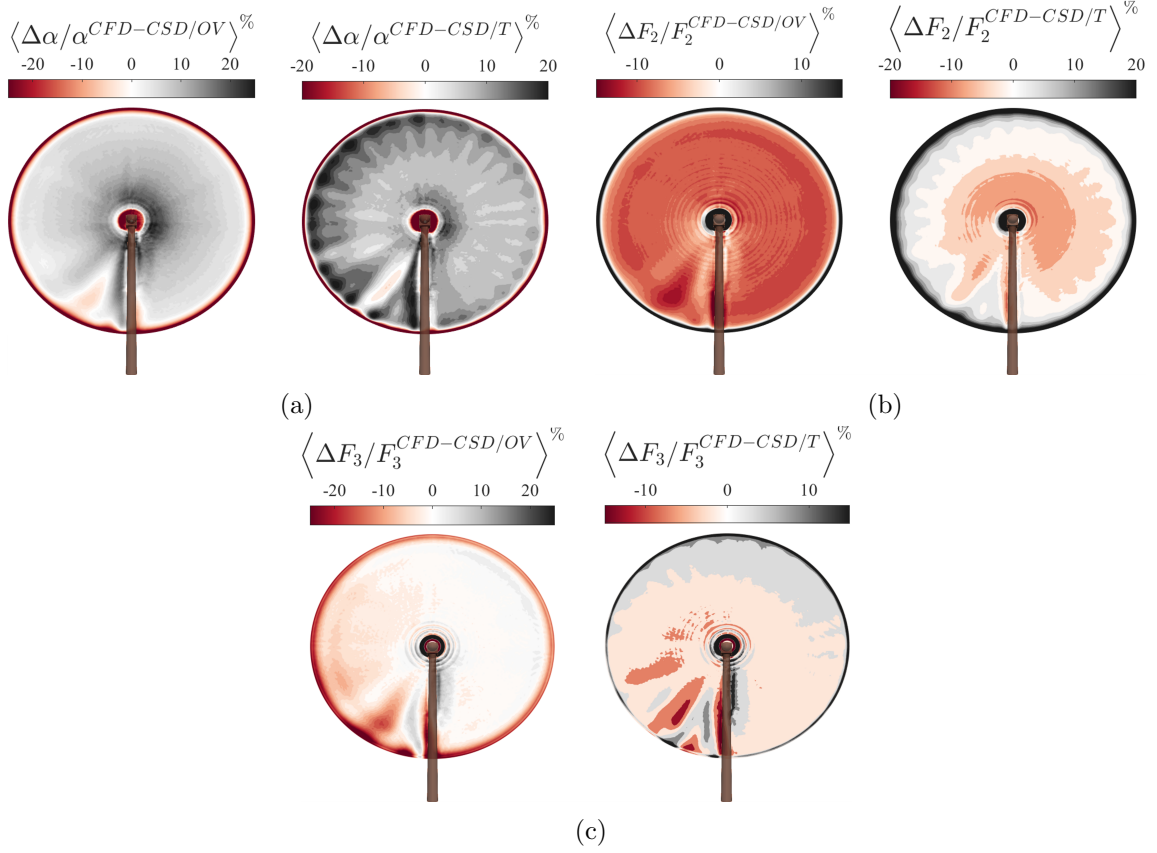


Figure 9: Phase-averaged contour plots of the percentual differences of the aerodynamic quantities between CFD-CSD/OV versus *ElastoDyn* (left), and CFD-CSD/T versus *BeamDyn* (right), respectively. (a) Incidence angle, (b) flapwise aerodynamic force, (c) edgewise aerodynamic force.

signals, especially concerning the angle of attack ($\approx 8\%$ of error) and the edgewise aerodynamic force at azimuthal angles close to zero ($\approx 6\%$ of error). Again, this observation indicates that including the torsional degree of freedom in the structural solver is crucial for describing accurately the amplitude and dynamical behaviour of the aerodynamic quantities.

4.3 Power and thrust coefficients

The aerodynamic loads previously presented are also useful to evaluate the power and thrust coefficients, defined as follows:

$$C_p = \frac{P_d}{\frac{1}{2}\rho AU_\infty^3}, \quad C_t = \frac{T_{aero}}{\frac{1}{2}\rho AU_\infty^2}, \quad (9)$$

where $A = \pi D^2/4$ represents the rotor area, P_d is the aerodynamic power transferred to the rotor and T_{aero} is the overall aerodynamic thrust on the turbine.

Starting from the time history of C_p and C_t , we computed their phase-averaged evolution as reported

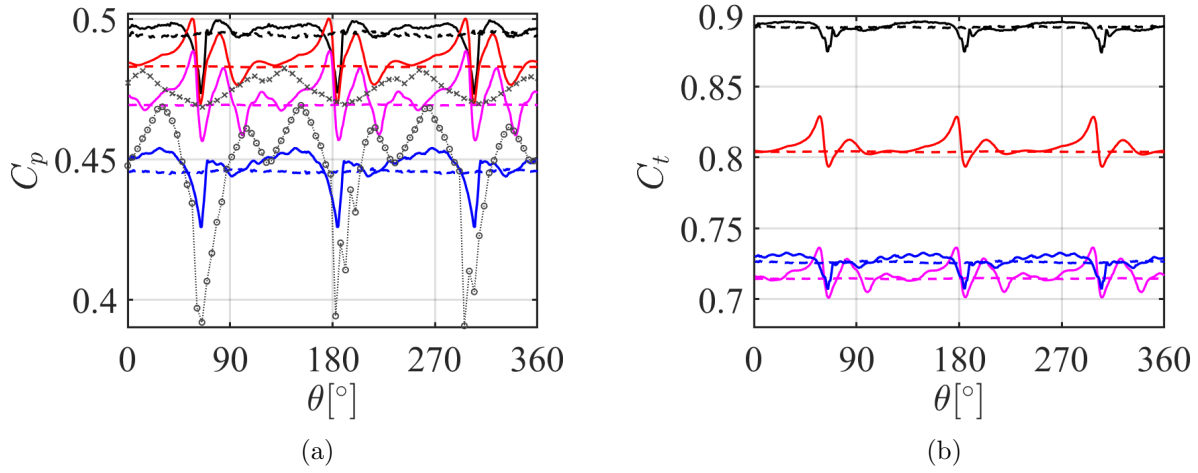


Figure 10: Phase-averaged power (a) and thrust (b) coefficients. CFD-CSD/OV: TN —, RO ----. CFD-CSD/T: TN —, RO ----. *ElastoDyn*: TN —, RO ----. *BeamDyn*: TN —, RO ----. From figure 3 of Bernardi et al. (2023): \circ *LES + CSD flexible*, \times *OpenFAST-AeroDyn*.

in Figure 10. The periodic passage of the blades in front of the tower for the TN configuration produces a drop of the curves of about 10%. Eventually, the performance is restored to the value obtained in the RO case following the elastic dynamical behavior of the structure. The results reflect the dependency of the power and thrust coefficients on the edgewise aerodynamic force F_3 and the flapwise aerodynamic force F_2 at the 80% of the blade, respectively (see Figures 8c and 8b), which are strongly influenced by the presence of the tower. Notice that, also here, we can observe that the drop in the C_p curve appears to be rather similarly predicted by BEM and CFD, although the BEM prediction exhibits notable oscillations before and after the drop, whereas these are not present in the CFD results. A different behaviour was observed for the NREL 5-MW turbine (as in figure 3 of Bernardi et al. (2023), included in Figure 10 of the present paper with symbols), where this performance drop is considerably underestimated by the BEM computations. A possible factor that may contribute to this different behaviour may reside in the different relative geometry of the two wind turbines. Indeed, the flow induced by a thinner tower (in diameter units), as in the case of the 15-MW wind turbine, might be better described by a potential flow solution compared to the one induced by a thicker tower, as in the case of the 5-MW wind turbine, and may thus lead to the observed improved agreement between BEM and CFD results. Moreover, the differences in the flow impinging on the blade might also have an effect. In fact, in Bernardi et al. (2023) a uniform inflow was imposed. Whereas, in the present case, due to the shear imposed at the inflow and the limited distance from the ground of the tip of the blade (only $\approx 0.125D$ for the 15MW turbine), the blade is invested by a flow having a much smaller velocity compared to the given value of U_∞ at hub height, further confirming the increased suitability of a potential flow solution upstream of the tower. Nevertheless, we should recall that this remains a very strong approximation, as also demonstrated by the differences in the forces and angles that have been observed in the previous section (see Figure 9, for instance).

It can be concluded that the performance loss induced by the passage in front of the tower is less

pronounced for the 15 MW NREL turbine in the present configuration ($\approx 5\%$) compared to the 5 MW turbine in the configuration considered in Bernardi et al. (2023) ($\approx 15\%$, see figure 3 of this reference), with both BEM theory and CFD yielding similar predictions in the case of the 15 MW turbine. However, it is worth recalling again that Bernardi et al. (2023) considered a uniform inflow, whereas here the inflow is sheared. This can be a possible reason for this different behaviour, since the lower wind speed in the lower part of the rotor plane leads to a lower production in the bottom half of the rotor plane, where the tower is located. This may cause a smaller performance drop due to the tower relative to the total produced power. Therefore, the observed difference can be not only due to the change in turbine size, but also due to the change in inflow conditions.

Moreover, the present results predict that, for very large rotors and a sheared inflow, the tower effect on blade deformations is less pronounced than for smaller rotors, although it should yet be taken into account for accurately describing the turbine's performance oscillations as it still represents a major source of unsteadiness.

The average value of the power coefficient is much larger when the torsional deformation is neglected. This feature is **observed** by both CFD and BEM approaches. However, one can observe that *ElastoDyn* underestimates the value of C_p with respect to the corresponding non-torsional CFD model, while the opposite is observed when comparing *BeamDyn* with the torsional CFD solver. This is **probably** due to the fact that *BeamDyn* predicts higher values of the aerodynamic **edgewise** forces with respect to the CFD-CSD/T approach, which are linked to a smaller torsional deformation as will be shown in figure 12f in the next section.

Figure 11 shows the premultiplied Power Spectral Density (PSD) of the power (Figure 11a) and thrust (Figure 11b) coefficients evolution. The PSD is normalized by the variance of each coefficient σ^2 and plotted versus the frequency normalized by the rotational frequency of the rotor, f/f_{rot} where the latter is denoted as $1P = f_{rot} = 7.5RPM$ and its multiples will be denoted as $2P, 3P$ etc. In both cases, the CFD-CSD solvers seem to provide a richer representation of the aerodynamic coefficients, capturing the full range of flow-structure interactions. Indeed, an examination of the low-frequency behavior reveals that both quantities exhibit isolated low-frequency peaks when using the BEM-based solvers, a phenomenon not observed with the CFD-CSD, where the low-frequency range is rather broadband and does not present particular peaks. It is important to notice that the frequency $1P$ can be directly linked to the frequency of the passage of the blade in front of the tower, but also to wind shear loads on the blades. Concerning the first point, a potential flow solution as that used in the BEM solver is keen to provide a simple, single-frequency response, whereas a complex, turbulent flow is expected to result in a more broadband spectrum. Concerning the second point, we have to consider that in LES, the power law profile is imposed at the inlet of the domain but it is free to evolve for 4 diameters before the wind turbine, altering in a non-trivial way the flow field and the consequent frequency response of the blades. This outcome indicates that the BEM-based solvers tend to overcut the power oscillations associated with low-frequencies that are not exactly equal to $1P$ or $2P$. For all solvers, however, the strongest PSD peaks are to be found at much larger frequencies ($3P$ - $6P$ - $9P$ - $12P$), as also observed by Pagamonci et al. (2023) by means of URANS aeroelastic simulations of the NREL 5-MW, the DTU 10-MW, and the IEA 15-MW turbines. One can also notice that the amplitude associated with the $3P$ frequency appears to be consistently described by the two solvers, although also in this range the BEM solver appears to overdamp the frequencies in between different peaks.

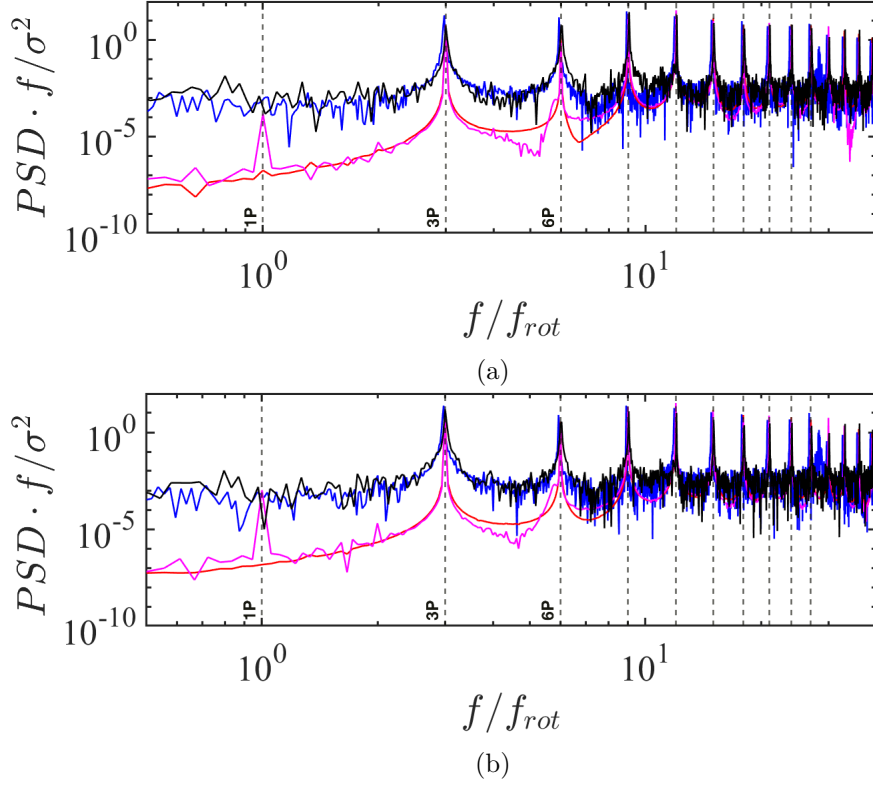


Figure 11: Power Spectral Density (PSD) of the power (a) and thrust (b) coefficients. The vertical dashed lines highlight the rotational frequency of the rotor $1P = f_{rot} = 7.5RPM$ and the multiples of $3P$, respectively. CFD-CSD/OV —, CFD-CSD/T —, *ElastoDyn* —, *BeamDyn* —.

Moreover, a good agreement is evident between the two set of results concerning the value of the frequencies and the level of the PSD for frequencies that are multiples of $3P$.

4.4 Structural response

This section presents the analysis of the structural dynamics. Figure 12 reports the phase-averaged dynamic response of the free extremity of the blade (left column) and the time-averaged deformation of the entire span (right column). Figure 12a shows how the out-of-plane deformation is mainly governed by the aerodynamic component of the force normal to the rotor plane and, hence, to the aerodynamic effects, heavily affected by the tower. In fact, it is visible how the tower placed at $\theta = 180^\circ$ produces a drop in the deformation, followed by an elastic dynamic response which restores the value far from the pointing-down position. The time-averaged maximum deformation predicted by the CFD-CSD/OV solver is 16% higher compared to the *ElastoDyn* module and 17% compared to *BeamDyn* (see Figure 12b). On the other hand, the same quantity predicted by the CFD-CSD/T solver is 17% lower compared to the *ElastoDyn* module and 13% compared to *BeamDyn* (see Figure 12b). This is consistent with the fact that including the torsional degree of freedom reduces the loads

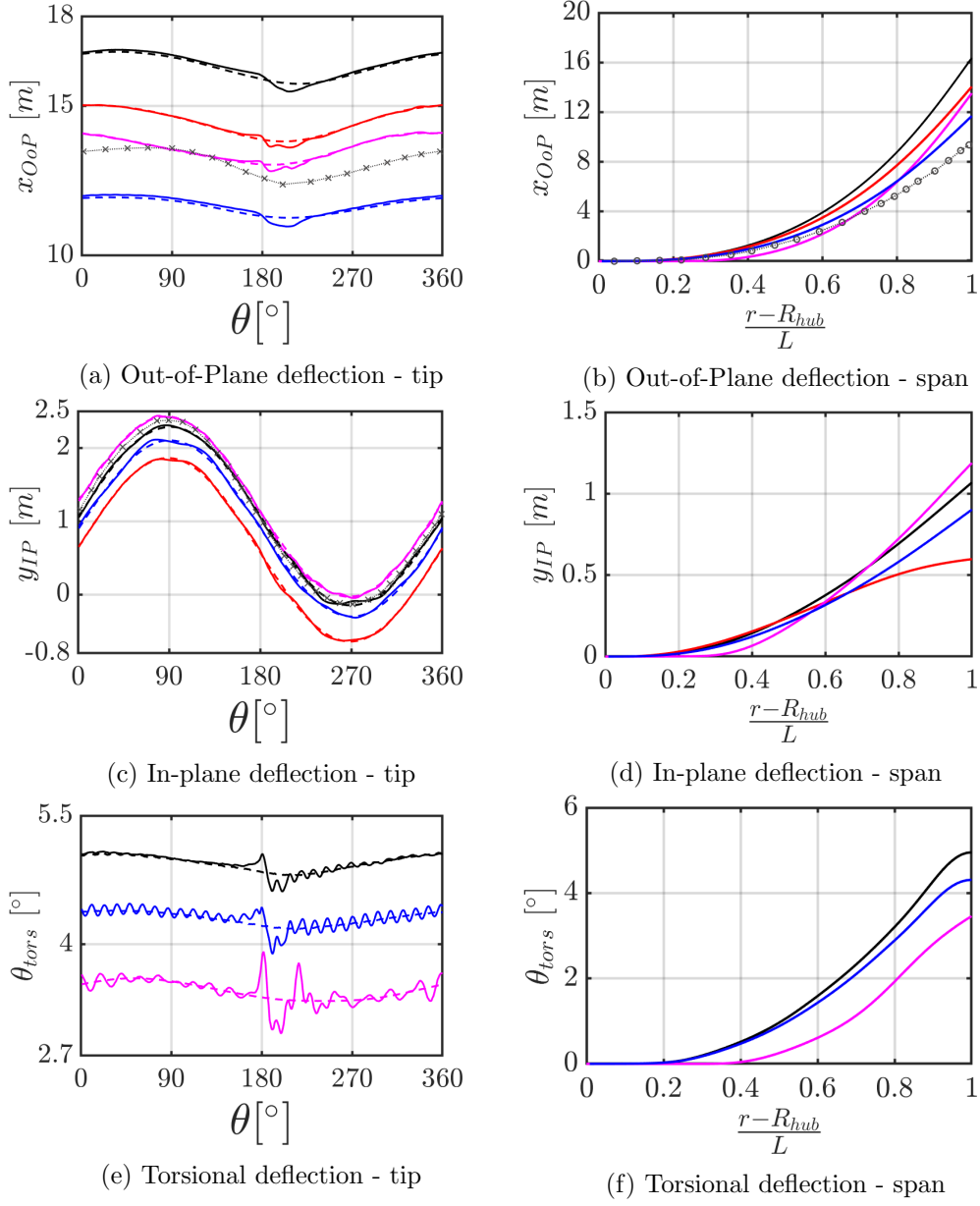


Figure 12: Phase-averaged deflections at the tip of the blade (left column) and time-averaged deflections along the blade span (right column). CFD-CSD/OV: TN —, RO ----. CFD-CSD/T: TN —, RO ----. *ElastoDyn*: TN —, RO ----. *BeamDyn*: TN —, RO ----. From figure 13 of Pagamonci et al. (2023) \circ , and figure 7a and 7b of Trigaux et al. (2024) \times .

(see figure 8b) and the resulting deformation. Although the trend of deformation with respect to the blade span appears similar to previous predictions based on URANS (see Pagamonci et al. (2023)),

the out-of-plane deformation is rather larger, reaching 16 m at the blade’s tip. The amplitude of the deformation is however **close to** that obtained by Trigaux et al. (2024) using LES. Figure 12c depicts instead the in-plane deformation, which is mostly due to gravity. The results show that the shadowing effect of the tower does not influence this quantity, **which is expected as the lag deformation is mainly driven by gravity**. Furthermore, the discrepancies obtained between *ElastoDyn* and *BeamDyn* can be attributed to the lack of modes used by the former model to describe the translation in the edgewise direction (see Figure 12d). The discrepancy does not seem to be linked to the linearity of this model, as the result of the CFD-CSD/T solver, which is linear as well, is much closer to the *BeamDyn* results. Moreover, the results of the CFD-CSD/OV and the CFD-CSD/T models are very **close each other**. It can be noticed that the amplitude of the oscillation of the in-plane deflection is consistent with that reported by Trigaux et al. (2024) **(see Figure 7b of their paper, reporting an oscillation between ≈ -2.3 and ≈ 0.2)**, although the sign is opposite due to the different frame of reference used.

A further significant insight into the deformation phenomenon is provided by the torsional DoF. Figure 12e shows a comparison of the torsional angle at the tip with *BeamDyn*. Significant discrepancies can be observed between the LES and the BEM approaches, which cannot be reconducted to the different coupling procedures adopted by the models. On the one hand, *BeamDyn* and CFD-CSD/T both take into account the deformation angle in the coupling (Wang et al., 2016b), while in the CFD-CSD/OV solver the angle of attack depends only on the deformation velocity (see Equation 8). However, the gap between the BEM and the CFD-CSD/T curves is quite large, reaching approximatively 20% of the torsional deformation value. These differences likely arise from the combined effects of both aerodynamic and structural modeling approaches used in BEM and LES. **Although in the present paper we have mostly focused on a comparison of the structural models, a thorough comparison of the aerodynamics modeling can be found in the report of IEA Task 47 Schepers et al. (2025), where results produced with the present code are included (see, for instance, figure 4.25 and following for non flexible blades).** The discrepancy between the BEM and the CFD-CSD results is confirmed by the time-averaged torsional deformation along the span reported in Figure 12f where the maximum percentual gap of *BeamDyn* reaches 29% for the CSD-CFD/OV, and 24% for the CFD-CSD/T. It is noteworthy that the lower torsional deformation resulting from *BeamDyn* leads to the higher aerodynamic loads observed in figure 8c.

Finally, figure 13 illustrates the Power Spectral Density (PSD) of the blade’s tip deformation components for the TN configuration (which is characterized by more complex fluid-structure interactions). The premultiplied PSD values are normalized by the variance of the signal, σ^2 , and plotted versus the frequency normalized by the rotor frequency, f/f_{rot} . Spectral results have been corroborated through use of the Welch and Lomb-Scargle PSD estimation algorithms.

Figure 13a shows the out-of-plane deformation, which we showed to be influenced mostly by the aerodynamic loading. The results indicate that, for all the numerical approaches used, the observed structural response does not exhibit a peak corresponding to the first flapwise natural frequency, suggesting that the intrinsic dynamics of the structure might play a less prominent role in the deformation process. **A similar behavior is found in** the results of Trigaux et al. (2024) **(see figure 6 of the cited paper)** for the same turbine and similar inflow conditions. **Noticeably, all the numerical models recovered peaks at frequencies close to the (highly damped) second and third flapwise natural frequencies, but they appear to rather correspond to the 13^{th} and 26^{th} multiple of the rotational fre-**

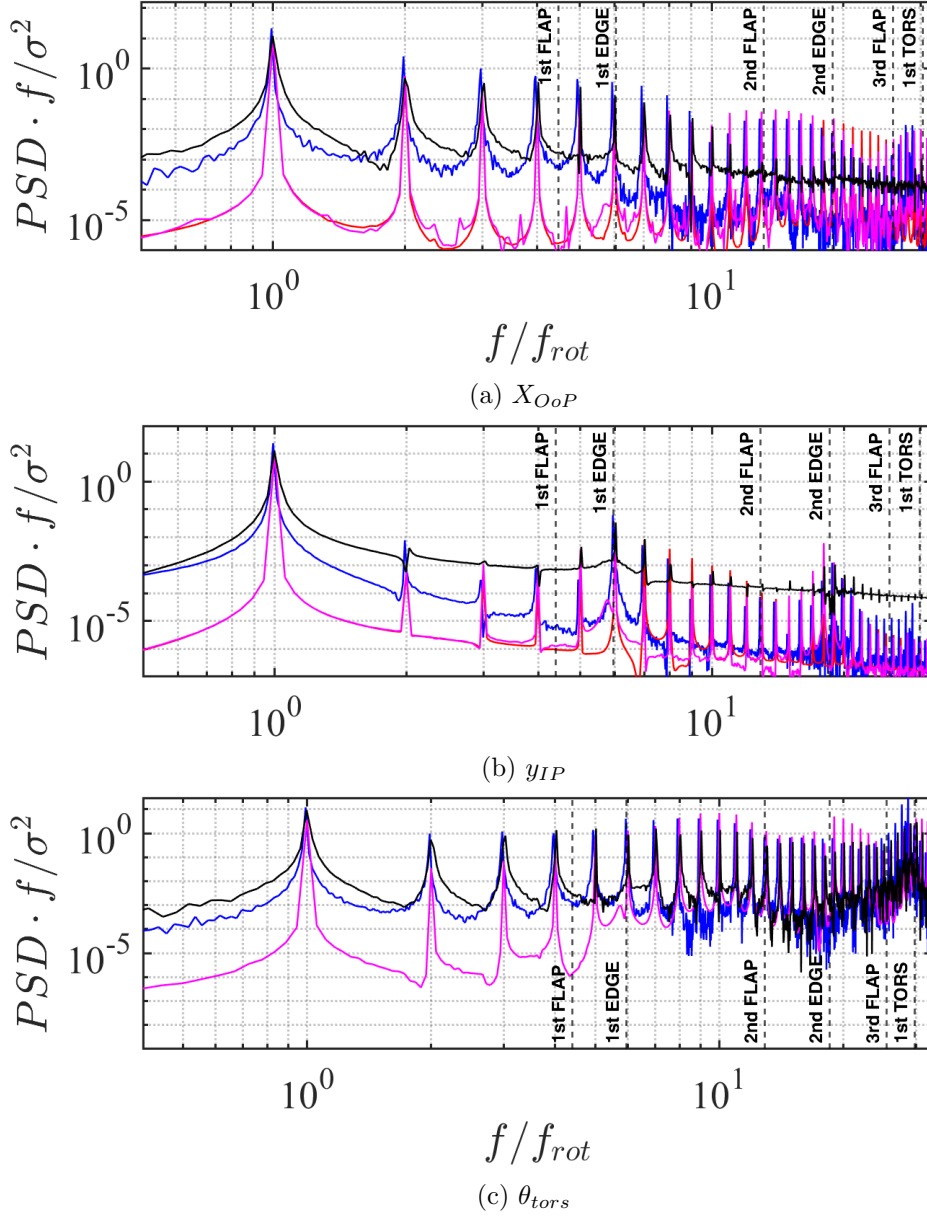


Figure 13: Power Spectral Density (PSD) of the out-of-plane (a), in-plane (b), and torsional (c) deformations of the blade. The vertical dashed lines represent the first 8 eigenfrequencies of the system. CFD-CSD/OV —, CFD-CSD/T —, *ElastoDyn* —, *BeamDyn* —.

quency (i.e., 13p and 26p). Both CFD-CSD solvers predict larger amplitude responses across a broad frequency range compared to OpenFAST, indicating a higher capability to capture complex flow interactions, including turbulence-induced vibrations. This effect is particularly pronounced at the lower frequencies, probably due to the large-scale three-dimensional structure of the flow impinging on the

turbine, which is not captured by OpenFAST, also due to the fact that the impinging flow on the turbine is purely two-dimensional, while it is not for CFD. For this reason, these aspects seem to be under-represented in the *ElastoDyn* and *BeamDyn* solutions. Although the *ElastoDyn* curve aligns with both the CFD-CSD solvers at some key frequency peaks, it does not account for the fine-scale flow-structure interactions. On the other hand, the *BeamDyn* curve provides better agreement with the CFD-CSD solvers, especially at higher frequencies near the blade’s natural modes, suggesting that *BeamDyn* captures more of the structural dynamics, particularly the aeroelastic response, probably due to its nonlinearity or to the number of degrees of freedom considered. Figure 13b shows the in-plane deformation, which is primarily influenced by gravity, centrifugal, and Coriolis forces acting on the blade. The CFD-CSD solvers again demonstrate stronger low-frequency components. Figure 13c presents the torsional deformation for the CFD-CSD/T and *BeamDyn* solvers, excluding *ElastoDyn*, which neglects the torsional DoF in the model. Additionally, also this quantity demonstrates that the CFD-CSD curves predict higher amplitudes at low frequencies. However, a good agreement between the two solvers is evident at higher frequencies, especially in the range around the first torsional eigenfrequency.

5 Conclusions

This study investigated the aeroelastic response of the IEA 15-MW wind turbine by employing a high-fidelity Computational Fluid Dynamics (CFD) solver that couples Large-Eddy Simulation (LES) with a Computational Structural Dynamics (CSD) solver. Two different CSD solvers are considered: the CFD-CSD/OV solver, in which the only structural quantity contributing to the definition of the angle of attack is the deformation velocity, and the CFD-CSD/T solver, in which the instantaneous torsional deformation is also considered when defining the local effective incidence. The results of the two CFD-CSD solvers are compared with those of traditional engineering solvers such as *BeamDyn* and *ElastoDyn*, both relying on Blade Element Momentum (BEM) theory. Two case studies were examined: a rotor-only configuration (RO) and one that included the tower and nacelle (TN).

In the first instance, a flow analysis uncovered important considerations regarding wake entrainment. In particular, the study found that, for the considered turbine, impinged by a laminar sheared inflow, wake recovery is only slightly hindered by the presence of the tower. The entrainment of kinetic energy driven by the tower leads to higher turbulence levels in the near wake, but then result into a slightly decreased mixing behind the turbine, differently to what has been found for the NREL 5MW wind turbine, whose wake recovery was found to be promoted by the presence of the tower. This result requires further examination, as it appears counter-intuitive and has not yet been confirmed by other studies.

In addition, the Power Spectral Density (PSD) of the power and thrust coefficients revealed that the CFD-CSD solver captures a broader range of flow-structure interactions, with a more broadband low-frequency response, compared to the BEM-based solvers. The isolated low-frequency peaks found in *BeamDyn* and *ElastoDyn* suggest that these solvers tend to over-simplify the aerodynamic fluctuations associated with phenomena such as wind shear and tower shadowing. For the large IEA 15-MW turbine, the performance drop caused by tower passage is not very pronounced and the resulting oscillations predicted by the BEM approach appear to be larger than the CFD-CSD solver.

Concerning the forces on the blade and the incidence angle, one can observe a rather good match between the CFD-CSD/OV solver and *ElastoDyn*, as well as between the CFD-CSD/T model and the *BeamDyn* solver. This is likely due to the presence – or not – of the torsional feedback, while non-linearities of the structural solver appear to have only a limited impact on the observed quantities. In agreement with previous studies, the results thus suggest that including the torsional degree of freedom in the structural solver is crucial for accurately describing the amplitude and dynamical behaviour of the aerodynamic quantities.

Moreover, it is observed that duly taking into account the torsional degree of freedom reduces the value of C_p . This feature is consistently observed by both CFD and BEM approaches. However, one can observe that *BeamDyn* predicts lower values of the torsional deformation and thus higher values of the aerodynamic **edgewise** forces with respect to the CFD-CSD/T approach, leading to a larger C_p value than that predicted by LES. **All in all, it can be concluded that for the considered setup, the CFD-CSD solvers tend to exhibit larger amplitudes at lower frequencies with respect to BEM ones.**

The structural response of the wind turbine blade has been assessed by comparing the out-of-plane, in-plane, and torsional deformations obtained from the CFD-CSD solvers, *ElastoDyn*-based, and *BeamDyn*-based OpenFAST solver. In-plane deformation, influenced significantly by centrifugal forces, appears to be better captured by the CFD-CSD solvers, especially in the low-frequency range. Concerning the out-of plane deflection, large discrepancies are seen between the two CFD-CSD solvers, as well as between both BEM modules and the LES.

Our results underscore the importance of incorporating torsional deformation effects in the definition of the angle of attack and using high-fidelity aeroelastic models to ensure accurate predictions of wind turbine blade performance with a richer fluid dynamics. Whereas, the linearity of the structural model does not appear to have a strong effect on the aerodynamical quantities, deformations and loads. In general, the comparison of the results of the CFD-CSD solver with those of the engineering solver shows differences especially in the region behind the tower. **The observed differences likely stem from the combined effects of differences in aerodynamic and structural fidelity, and cannot be uniquely attributed to one component alone.**

Future work will explore the effect of turbulent fluctuations at the inlet to better investigate the impact of the atmospheric boundary layer on the aerodynamic forces, loads and deformations of the present turbine.

A Appendix A. **Grid convergence study for LES**

A grid convergence study was conducted to evaluate the sensitivity of the LES results to spatial and temporal resolution. Two **further** simulations were carried out using grids of different densities: **a coarser mesh and a finer mesh, having approximately 40% less and more grid points than the former in each spatial direction, respectively.** This allowed for a more detailed resolution of flow structures and aerodynamic quantities. Moreover, **both simulations** use the same $CFL = 0.65$ as the present grid. The average time step obtained and the other key parameters of **different** LES runs are summarized in Table A1.

The comparison in figure A2 shows that the results obtained using the coarse and fine grids are extremely close **to** each other along the entire blade span. In particular, the curves of the angle of

| Parameter | Coarse Grid | Present Grid | Fine Grid |
|----------------------------|--------------------|--------------------|--------------------|
| Total number of cells | 1.31×10^8 | 5.37×10^8 | 1.36×10^9 |
| Largest cell diagonal (m) | 8.1 | 5.0 | 3.5 |
| Smallest cell diagonal (m) | 3.9 | 2.5 | 1.7 |
| Actuator points per blade | 54 | 86 | 128 |
| Average time step (s) | 0.043 | 0.024 | 0.012 |
| Total number of threads | 320 | 512 | 768 |

Table A1: Comparison of the main parameters for different meshes.

attack are almost indistinguishable for the coarser and the reference grid, even in the outer portion of the blade, where stronger differences were expected due to tip effects and local three-dimensionality. Slightly larger differences are recovered between the reference and the finer grid, but only at low radius. In particular, for these two grids the maximum deviation of the incidence angle α between the two simulations at 80% of the span reaches a value of $\Delta\alpha_{max} \approx 0.2^\circ$, corresponding to a relative difference of 1.6%. Whereas, the maximum deviation between the reference and the coarser grids at 80% of the blade span is $\Delta\alpha_{max} \approx 0.1^\circ$, corresponding to a relative difference of 1.5%. Similarly, the aerodynamic forces component distributions exhibit negligible variation between the reference and finer resolutions, and less than 1% relative variations between the reference and the coarser grids, confirming the overall consistency of the LES solution examined in the Sec. 4 with respect to mesh refinement.

These results indicate that the coarse grid already accurately captures the main aerodynamic features, making the use of a finer mesh unjustified given its higher computational cost and minimal accuracy gain.

B Appendix B. Validation of the structural model

The structural model for the IEA 15MW wind turbine has been cross-validated with many other aeroelastic numerical codes within the framework of the International Energy Agency (IEA) Wind TCP Task 47 TURBINIA (Schepers et al., 2025). In this IEA Task, a consortium of research institutions and industrial partners benchmarked their own aeroelastic codes on the IEA 15 MW wind turbine (Cacciola et al., 2025). Since we cannot report in this paper data from all these partners, we provide here a preliminary study was conducted to validate the structural model prior to coupling it with the CFD solver. Figure B1 shows the distributions of the structural and constructive properties along the blade, which were utilized as input for the modal CSD analysis. A convergence study to determine the proper number of elements, N_e , (not reported here for brevity) was conducted, leading to the choice $N_e = 80$. Furthermore, the results of the present structural analysis were compared with those of five models including: the prismatic Timoshenko model without torsion (H2-PTNT); the Timoshenko model with a fully populated stiffness matrix (H2-FPM) from the study of Rinker et al. (2020); the 3D Finite Element Analysis (3D FEA) selected from Zhang et al. (2023); the ElastoDyn model; the BeamDyn model. Figure B2 shows the first 8 eigenfrequencies using the present method compared

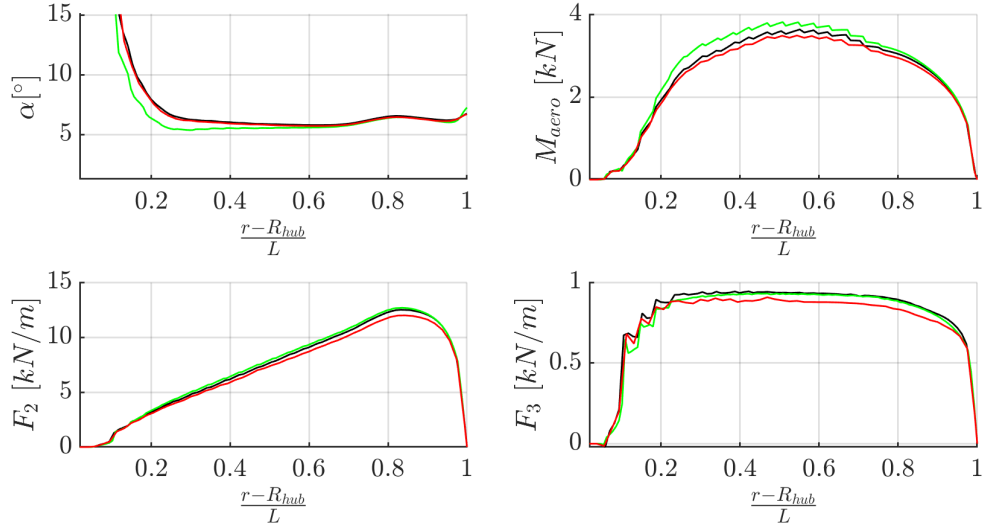


Figure A1

Figure A2: Average aerodynamic quantities along the blade obtained from the **coarse grid (red line)**, **the present grid (black line)** and **the finer grid (green line)**. (top left) Incidence angle, (top right) Aerodynamic pitch moment, (bottom left) flapwise aerodynamic force, (bottom right) edgewise aerodynamic force.

with the results of these models. The computed values of the modal frequencies appear to be consistent with the other results, although some discrepancies in the higher-order modes are observed. Moreover, an analysis of the most important modes was conducted: Table B1 provides the classification of the first 8 modes, whereas, Figures B3, B4, and B5 show the modal displacements for the first spanwise, edgewise, and torsional modes, respectively.

| # | $f_n[Hz]$ | Mode |
|---|-----------|---------------|
| 1 | 0.5369 | 1st flapwise |
| 2 | 0.7267 | 1st edgewise |
| 3 | 1.577 | 2nd flapwise |
| 4 | 2.267 | 2nd edgewise |
| 5 | 3.113 | 3rd flapwise |
| 6 | 3.642 | 1st torsional |
| 7 | 4.571 | 3rd edgewise |
| 8 | 5.385 | 4th flapwise |

Table B1: Classification of the first 8 structural modes.

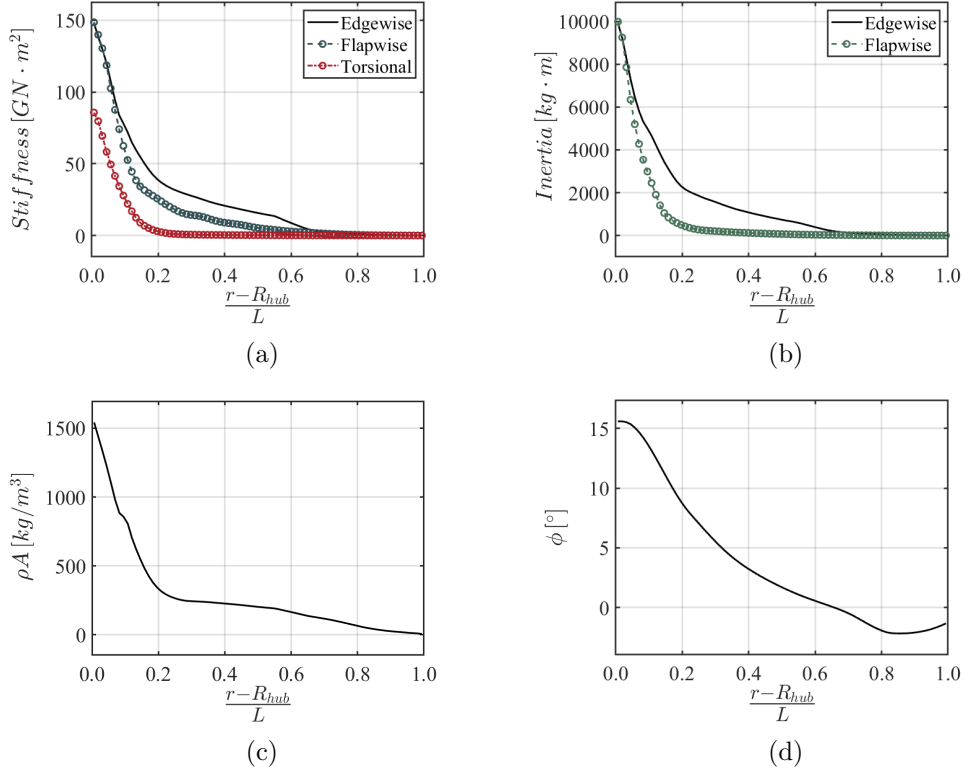


Figure B1: Structural properties of the blade along the span: (a) stiffness, (b) inertia, (c) density, (d) local twist angle.

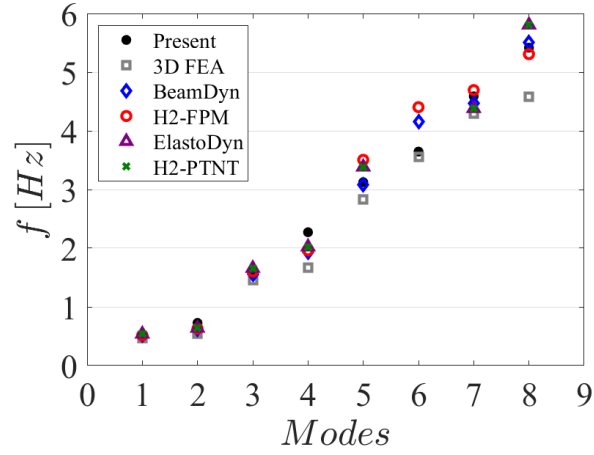


Figure B2: A comparison of the eigenfrequencies computed by different structural models.

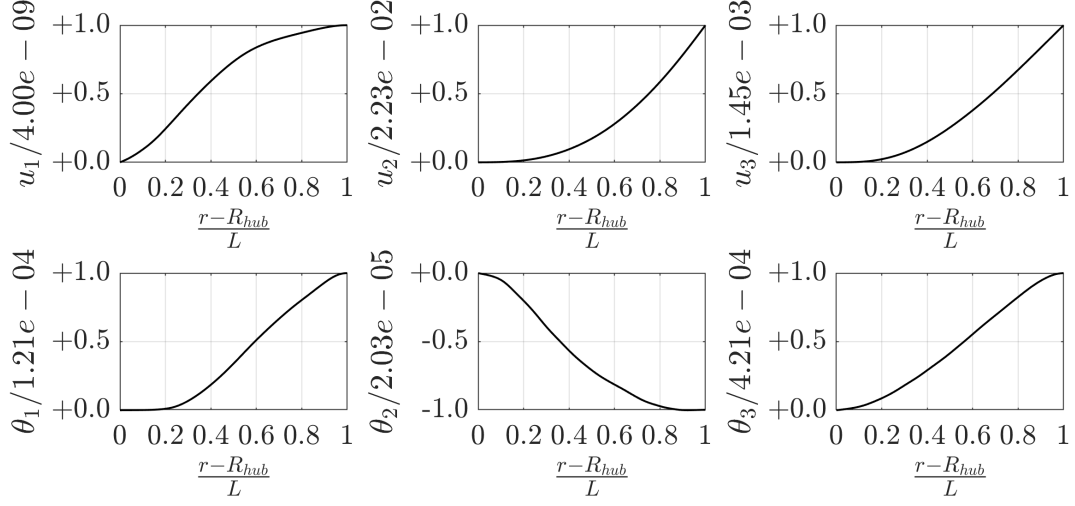


Figure B3: Mode 1 shape for all the DoFs.

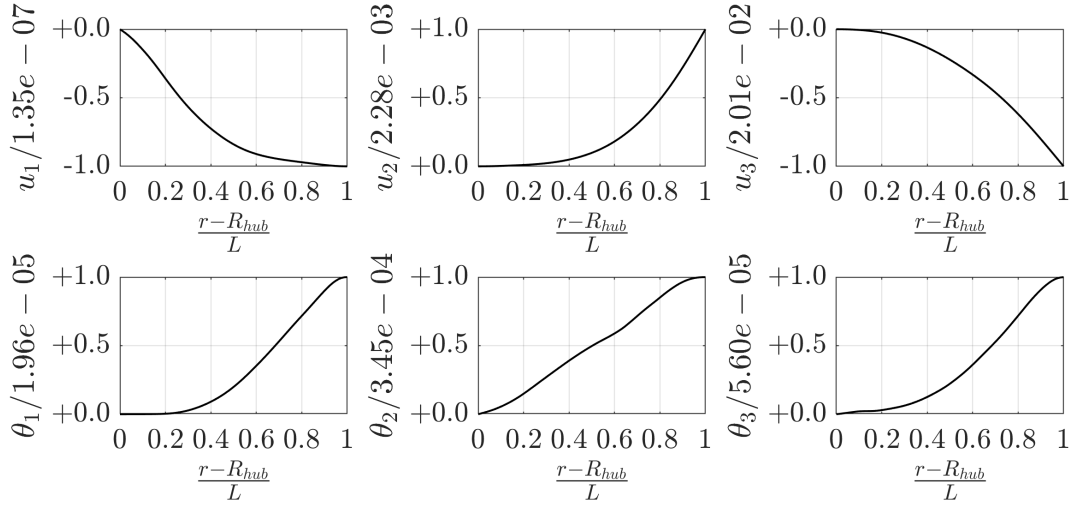


Figure B4: Mode 2 shape for all the DoFs.

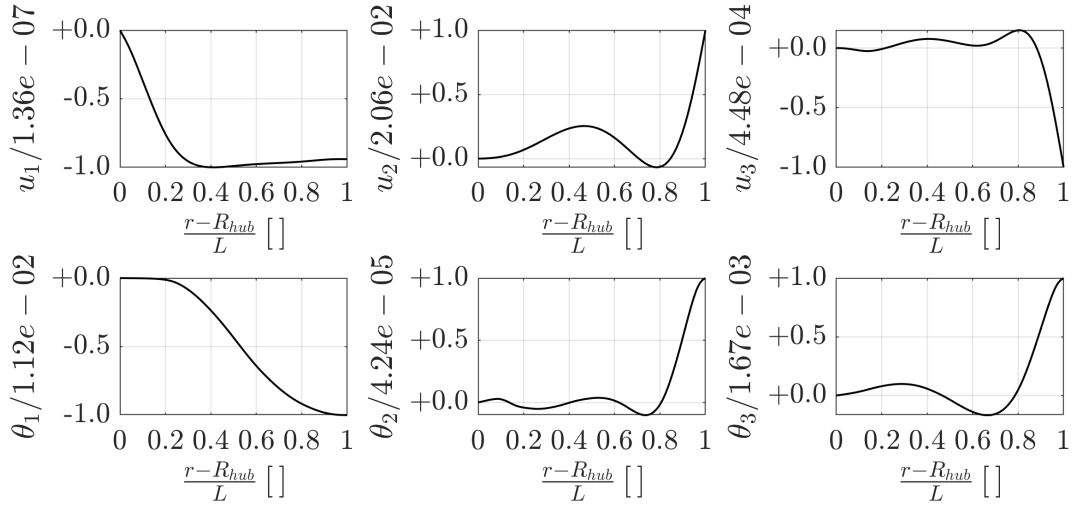


Figure B5: Mode 6 shape for all the DoFs.

688 *Author contribution.* CB: Investigation, Writing - Original draft, Formal analysis, Methodology, Soft-
689 ware, Validation. SC: Conceptualization, Investigation, Writing - Review & Editing, Supervision. FM:
690 Methodology, Software, Validation. GDP: Formal analysis, Writing - Review & Editing, Methodol-
691 ogy, software. SL: Conceptualization, Software, Supervision. PDP: Conceptualization, Investigation,
692 Writing - Review & Editing, Supervision.

693 *Competing interests.* The authors declare that they have no competing interests.

694 *Acknowledgments.* This study has been partially funded under the National Recovery and Resilience
695 Plan (NRRP), Mission 4 Component 2 Investment 1.3 - Call for tender No. 1561 of 11.10.2022
696 Project code PE0000021, Project title "Network 4 Energy Sustainable Transition – NEST", and
697 under the PRIN grant 20229YJP33, "Diffuser augmented Wind Turbines for URBan environments"
698 (DWTURB). Both are grants of Ministero dell'Università e della Ricerca (MUR), funded by the
699 European Union – NextGenerationEU. The cooperative work on the 15MW NREL wind turbine
700 within the IEA WIND TASK 47 - TURBINIA is also acknowledged.

701 References

- 702 Abdel Hafeez, M. M. and El-Badawy, A. A.: Flutter limit investigation for a horizontal axis wind tur-
703 bine blade, *Journal of Vibration and Acoustics*, 140, 041 014, doi:<https://doi.org/10.1115/1.4039402>,
704 2018.
- 705 Allah, V. A. and Sha ei Mayam, M. H.: Large Eddy Simulation of flow around a single and two in-line
706 horizontal-axis wind turbines, *Energy*, 121, 533–544, 2017.
- 707 Bartl, J. and Satran, L.: Blind test comparison of the performance and wake flow between two in-line
708 wind turbines exposed to different turbulent inflow conditions, *Wind Energy Science*, 2, 55–76, 2017.
- 709 Bayati, I., Belloli, M., Bernini, L., and Zasso, A.: Aerodynamic design methodology for wind tunnel
710 tests of wind turbine rotors, *Journal of Wind Engineering and Industrial Aerodynamics*, 167, 217–
711 227, doi:<https://doi.org/10.1016/j.jweia.2017.05.004>, 2017.
- 712 Bazilevs, Y., Hsu, M.-C., Kiendl, J., Wüchner, R., and Bletzinger, K.-U.: 3D simulation of wind
713 turbine rotors at full scale. Part II: Fluid-structure interaction modeling with composite blades,
714 *International Journal for Numerical Methods in Fluids*, 65, 236 – 253, doi:10.1002/fld.2454, cited
715 by: 441, 2011.
- 716 Bernardi, C., Posta, G. D., Palma, P. D., Leonardi, S., Bernardoni, F., Bernardini, M., and Cherubini,
717 S.: The effect of the tower's modeling on the aero-elastic response of the NREL 5 MW wind turbine,
718 *Journal of Physics: Conference Series*, 2505, 012037, doi:10.1088/1742-6596/2505/1/012037, URL
719 <https://dx.doi.org/10.1088/1742-6596/2505/1/012037>, 2023.

- 720 Boorsma, K., Greco, L., and Bedon, G.: Rotor wake engineering models for aeroelastic applications,
721 Journal of Physics: Conference Series, 1037, 062 013, doi:10.1088/1742-6596/1037/6/062013, URL
722 <https://doi.org/10.1088/1742-6596/1037/6/062013>, 2018.
- 723 Boorsma, K., Schepers, G., Aagard Madsen, H., Pirrung, G., Sørensen, N., Bangga, G., Imiela,
724 M., Grinderslev, C., Meyer Forsting, A., Shen, W. Z., Croce, A., Cacciola, S., Schaffarczyk,
725 A. P., Lobo, B., Blondel, F., Gilbert, P., Boisard, R., Höning, L., Greco, L., Testa, C.,
726 Branlard, E., Jonkman, J., and Vijayakumar, G.: Progress in the validation of rotor aerody-
727 namic codes using field data, Wind Energy Science, 8, 211–230, doi:10.5194/wes-8-211-2023, URL
728 <https://wes.copernicus.org/articles/8/211/2023/>, 2023.
- 729 Boorsma, K., Schepers, J. G., Pirrung, G. R., Madsen, H. A., Sørensen, N. N., Grinderslev,
730 C., Bangga, G., Imiela, M., Croce, A., Cacciola, S., Blondel, F., Branlard, E., and Jonkman,
731 J.: Challenges in Rotor Aerodynamic Modeling for Non-Uniform Inflow Conditions, Jour-
732 nal of Physics: Conference Series, 2767, 022 006, doi:10.1088/1742-6596/2767/2/022006, URL
733 <https://doi.org/10.1088/1742-6596/2767/2/022006>, 2024.
- 734 Burton, T., Jenkins, N., Sharpe, D., and Bossanyi, E.: Wind energy handbook, John Wiley & Sons,
735 2011.
- 736 Cacciola, S., Croce, A., Bangga, G., Pirrung, G., H., M., Sørensen, N., Grinderslev, G., Bonfils, N.,
737 Persent, E., Gilbert, I., Joulin, A., Greco, L., Aryan, N., Castorrini, A., Morici, A., Chetan, M.,
738 Jonkman, J., Branlard, E., Cherubini, S., Bernardi, C., Boorsma, K., Schepers, J. D., Bianchini,
739 A., Pagamoci, L., Papi, F., Hach, O., Imiela, M., and Witt, D.: A Comparative Study of Different
740 Modeling Tools and Analysis Techniques for Aeroelastic Stability Assessment, in: submitted to The
741 Science of Making Torque from Wind, 2025.
- 742 Chen, X.: Experimental investigation on structural collapse of a large composite wind tur-
743 bine blade under combined bending and torsion, Composite Structures, 160, 435–445, doi:
744 <https://doi.org/10.1016/j.renene.2022.08.113>, 2017.
- 745 Chung, J. and Hulbert, G. M.: A Time Integration Algorithm for Structural Dynamics With Improved
746 Numerical Dissipation: The Generalized- α Method, Journal of Applied Mechanics, 60, 371–375, doi:
747 10.1115/1.2900803, URL <https://doi.org/10.1115/1.2900803>, 1993.
- 748 Ciri, U., Petrolo, G., Salvetti, M. V., and Leonardi, S.: Large-Eddy Simulations of Two In-Line
749 Turbines in a Wind Tunnel with Different Inflow Conditions, Energies, 10, 821, 2017.
- 750 Courant, R., Friedrichs, K., and Lewy, H.: On the partial difference equations of mathematical physics,
751 IBM journal of Research and Development, 11, 215–234, doi:<https://doi.org/10.1147/rd.112.0215>,
752 1967.
- 753 Damgaard, M., Ibsen, L. B., Andersen, L. V., and Andersen, J. K.: Cross-wind modal properties of
754 offshore wind turbines identified by full scale testing, Journal of Wind Engineering and Industrial
755 Aerodynamics, 116, 94–108, doi:<https://doi.org/10.1016/j.jweia.2013.03.003>, 2013.

756 Damiani, R., Jonkman, J., and Hayman, G.: SubDyn user’s guide and theory manual, Tech. rep.,
757 National Renewable Energy Lab.(NREL), Golden, CO (United States), 2015.

758 De Cillis, G., Semeraro, O., Leonardi, S., De Palma, P., and Cherubini, S.: Dynamic-mode-
759 decomposition of the wake of the NREL-5MW wind turbine impinged by a laminar inflow, Re-
760 newable Energy, 199, 1–10, 2022.

761 Della Posta, G., Leonardi, S., and Bernardini, M.: A two-way coupling method for the
762 study of aeroelastic effects in large wind turbines, Renewable Energy, 190, 971–992, doi:
763 <https://doi.org/10.1016/j.renene.2022.03.158>, 2022.

764 Della Posta, G., Leonardi, S., and Bernardini, M.: Large eddy simulations of a utility-scale horizontal
765 axis wind turbine including unsteady aerodynamics and fluid-structure interaction modelling, Wind
766 Energy, 26, 98–125, doi:<https://doi.org/10.1002/we.2789>, 2023.

767 Dong, X., Lian, J., Wang, H., Yu, T., and Zhao, Y.: Structural vibration monitoring and opera-
768 tional modal analysis of offshore wind turbine structure, Ocean Engineering, 150, 280–297, doi:
769 <https://doi.org/10.1016/j.oceaneng.2017.12.052>, 2018.

770 Gaertner, E., Rinker, J., Sethuraman, L., Zahle, F., Anderson, B., Barter, G., Abbas, N., Meng, F.,
771 Bortolotti, P., Skrzypinski, W., Scott, G., Feil, R., Bredmose, H., Dykes, K., Sheilds, M., Allen, C.,
772 and Viselli, A.: Definition of the IEA 15-Megawatt Offshore Reference Wind Turbine, Tech. rep.,
773 International Energy Agency, URL <https://www.nrel.gov/docs/fy20osti/75698.pdf>, 2020a.

774 Gaertner, E., Rinker, J., Sethuraman, L., Zahle, F., Anderson, B., Barter, G., Abbas, N., Meng, F.,
775 Bortolotti, P., Skrzypinski, W., et al.: Definition of the IEA 15-megawatt offshore reference wind
776 turbine, 2020b.

777 Hansen, M.: Aerodynamics of wind turbines, Routledge, 2015.

778 Hansen, M. H.: Aeroelastic instability problems for wind turbines, Wind Energy: An International
779 Journal for Progress and Applications in Wind Power Conversion Technology, 10, 551–577, doi:
780 <https://doi.org/10.1002/we.242>, 2007.

781 Heinz, J.: Partitioned Fluid-Structure Interaction for Full Rotor Computations Using CFD, Ph.D.
782 thesis, Denmark, 2013.

783 Jonkman, J.: The New Modularization Framework for the FAST Wind Turbine CAE Tool, doi:
784 [10.2514/6.2013-202](https://arc.aiaa.org/doi/abs/10.2514/6.2013-202), URL <https://arc.aiaa.org/doi/abs/10.2514/6.2013-202>, 2013.

785 Jonkman, J. M., Hayman, G., Jonkman, B., Damiani, R., and Murray, R.: AeroDyn v15 user’s guide
786 and theory manual, NREL Draft Report, 46, 2015.

787 Krogstad, P.-A., Satran, L., and Adaramola, M. S.: Blind Test 3: calculations of the performance
788 and wake development behind two in-line and offset model wind turbines, Journal of Fluids and
789 Structures, 52, 65–80, 2015.

790 Manwell, J. F., McGowan, J. G., and Rogers, A. L.: Wind energy explained: theory, design and
791 application, John Wiley & Sons, 2010.

792 Martinez-Tossas, L. A., Churchfield, M. J., Yilmaz, A. E., Sarlak, H., Johnson, P. L., Sørensen, J. N.,
793 Meyers, J., and Meneveau, C.: Comparison of four large-eddy simulation research codes and effects
794 of model coefficient and inflow turbulence in actuator-line-based wind turbine modeling, *Journal of*
795 *Renewable and Sustainable Energy*, 10, doi:<https://doi.org/10.1063/1.5004710>, 2018.

796 Moeller, T.: Blade cracks signal new stress problem, *WindPower Monthly*, 25, 1997.

797 Moriarty, P. J. and Hansen, A. C.: *AeroDyn Theory Manual*, doi:10.2172/15014831, 2005.

798 Orlandi, P.: *Fluid flow phenomena: a numerical toolkit*, vol. 55, Springer Science & Business Media,
799 2012.

800 Orlandi, P. and Leonardi, S.: DNS of turbulent channel flows with two-and three-dimensional rough-
801 ness, *Journal of Turbulence*, p. N73, doi:<https://doi.org/10.1080/14685240600827526>, 2006.

802 Pagamonci, L., Papi, F., Balduzzi, F., Xie, S., Sadique, J., Scienza, P., and Bianchini, A.: To what
803 extent is aeroelasticity impacting multi-megawatt wind turbine upscaling? A critical assessment,
804 in: *Journal of Physics: Conference Series*, vol. 2648, p. 012005, IOP Publishing, doi:10.1088/1742-
805 6596/2648/1/012005, 2023.

806 Pino Martín, M., Piomelli, U., and Candler, G. V.: Subgrid-scale models for compressible large-eddy
807 simulations, *Theoretical and Computational Fluid Dynamics*, 13, 361–376, 2000.

808 Porte-Agel, F. and Wu, Y.-T.: Large-Eddy Simulation of Wind-Turbine Wakes: Evaluation of Turbine
809 Parametrisations, *Boundary Layer Meteorology*, 138, 345–366, 2011.

810 Reschke, C.: Flight loads analysis with inertially coupled equations of motion, in: *AIAA Atmospheric*
811 *Flight Mechanics Conference and Exhibit*, p. 6026, doi:<https://doi.org/10.2514/6.2005-6026>, 2005.

812 Ribeiro, A. F. P., Casalino, D., and Ferreira, C. S.: Nonlinear inviscid aerodynamics of a wind turbine
813 rotor in surge, sway, and yaw motions using a free-wake panel method, *Wind Energy Science*, 8, 661–
814 675, doi:10.5194/wes-8-661-2023, URL <https://wes.copernicus.org/articles/8/661/2023/>,
815 2023.

816 Rinker, J., Gaertner, E., Zahle, F., Skrzypiński, W., Abbas, N., Bredmose, H., Barter, G., and
817 Dykes, K.: Comparison of loads from HAWC2 and OpenFAST for the IEA Wind 15 MW Reference
818 Wind Turbine, in: *Journal of Physics: Conference Series*, vol. 1618, p. 052052, IOP Publishing,
819 doi:10.1088/1742-6596/1618/5/052052, 2020.

820 Sabale, A. K. and Gopal, N. K. V.: Nonlinear Aeroelastic Analysis of Large Wind Turbines
821 Under Turbulent Wind Conditions, *AIAA Journal*, 57, 4416–4432, doi:10.2514/1.J057404, URL
822 <https://doi.org/10.2514/1.J057404>, 2019.

- 823 Saltari, F., Riso, C., Matteis, G. D., and Mastroddi, F.: Finite-element-based modeling for
824 flight dynamics and aeroelasticity of flexible aircraft, *Journal of Aircraft*, 54, 2350–2366, doi:
825 <https://doi.org/10.2514/1.C034159>, 2017.
- 826 Santoni, C., Ciri, U., Rotea, M., and Leonardi, S.: Development of a high fidelity CFD code
827 for wind farm control, in: 2015 American Control Conference (ACC), pp. 1715–1720, doi:
828 [10.1109/ACC.2015.7170980](https://doi.org/10.1109/ACC.2015.7170980), 2015.
- 829 Santoni, C., Carrasquillo, K., Arenas-Navarro, I., and Leonardi, S.: Effect of tower and nacelle on the
830 flow past a wind turbine, *Wind Energy*, 20, 1927–1939, doi:<https://doi.org/10.1002/we.2130>, 2017.
- 831 Santoni, C., García-Cartagena, E. J., Ciri, U., Zhan, L., Valerio Iungo, G., and Leonardi, S.: One-
832 way mesoscale-microscale coupling for simulating a wind farm in North Texas: Assessment against
833 SCADA and LiDAR data, *Wind Energy*, 23, 691–710, doi:<https://doi.org/10.1002/we.2452>, 2020.
- 834 Schepers, J., Boorsma, K., Madsen, H., Pirrung, G., Bangga, G., Guma, G., Lutz, T., Potentier, T.,
835 Braud, C., Guilmineau, E., Croce, A., Cacciola, S., Schaffarczyk, A. P., Lobo, B. A., Ivanell, S., As-
836 muth, H., Bertagnolio, F., Sørensen, N., Shen, W. Z., Grinderslev, C., Forsting, A. M., Blondel, F.,
837 Bozonnet, P., Boisard, R., Yassin, K., Hoening, L., Stoevesandt, B., Imiela, M., Greco, L., Testa, C.,
838 Magionesi, F., Vijayakumar, G., Ananthan, S., Sprague, M. A., Branlard, E., Jonkman, J., Carrion,
839 M., Parkinson, S., and Cicirello, E.: IEA Wind TCP Task 29, Phase IV: Detailed Aerodynamics of
840 Wind Turbines, doi:10.5281/zenodo.4813068, URL <https://doi.org/10.5281/zenodo.4813068>,
841 2021.
- 842 Schepers, J. G., Boorsma, K., Bois, R., Bangga, G., Jonkman, J., Kelley, C., Branlard, E.,
843 Gonçalves Pinto, W., Imiela, M., Hach, O., Greco, L., Testa, C., Aryan, N., Madsen, H., Croce, A.,
844 Cacciola, S., Pirrung, G., Sørensen, N., Grinderslev, C., Bernardi, C., Cherubini, S., Bianchini, A.,
845 Papi, F., Pagamonci, L., Braud, C., Höning, L., Theron, J., and Mohan, K.: Turbinia, turbulent
846 inflow innovative aerodynamics, Tech. rep., IEA Wind TCP–Task47, 2025.
- 847 Shen, W. Z., Mikkelsen, R., Sørensen, J. N., and Bak, C.: Tip loss corrections for wind turbine
848 computations, *Wind Energy: An International Journal for Progress and Applications in Wind*
849 *Power Conversion Technology*, 8, 457–475, doi:<https://doi.org/10.1002/we.153>, 2005.
- 850 Sorensen, J. and Shen, W. Z.: Numerical Modeling of Wind Turbine Wakes, *Journal of Fluids Engi-*
851 *neering*, 124, 393–399, doi:10.1115/1.1471361, URL <https://doi.org/10.1115/1.1471361>, 2002.
- 852 Sørensen, J. N.: Aerodynamic aspects of wind energy conversion, *Annual Review of Fluid Mechanics*,
853 43, 427–448, doi:<https://doi.org/10.1146/annurev-fluid-122109-160801>, 2011.
- 854 Stevens, R. J., Martinez-Tossas, L. A., and Meneveau, C.: Comparison of wind farm large eddy
855 simulations using actuator disk and actuator line models with wind tunnel experiments, *Renewable*
856 *Energy*, 116, 470–478, 2018.
- 857 Trigaux, F., Chatelain, P., and Winckelmans, G.: Investigation of blade flexibility effects on the loads
858 and wake of a 15 MW wind turbine using a flexible actuator line method, *Wind Energy Science*, 9,
859 1765–1789, doi:<https://doi.org/10.5194/wes-9-1765-2024>, 2024.

860 Troldborg, N.: Actuator line modeling of wind turbine wakes, Ph.D. thesis, Technical University of
861 Denmark, 2009.

862 Vermeer, L., Sørensen, J. N., and Crespo, A.: Wind turbine wake aerodynamics, *Progress in aerospace*
863 *sciences*, 39, 467–510, doi:[https://doi.org/10.1016/S0376-0421\(03\)00078-2](https://doi.org/10.1016/S0376-0421(03)00078-2), 2003.

864 Wang, L., Liu, X., and Kolios, A.: State of the art in the aeroelasticity of wind turbine
865 blades: Aeroelastic modelling, *Renewable and Sustainable Energy Reviews*, 64, 195–210, doi:
866 <https://doi.org/10.1016/j.rser.2016.06.007>, 2016a.

867 Wang, Q., Jonkman, J., Sprague, M., and Jonkman, B.: Beamdyn user’s guide and theory manual,
868 National Renewable Energy Laboratory, 2016b.

869 Yu, D. O. and Kwon, O. J.: Predicting wind turbine blade loads and aeroelastic response using a
870 coupled CFD-CSD method, *Renewable Energy*, 70, 184 – 196, doi:10.1016/j.renene.2014.03.033,
871 cited by: 111, 2014.

872 Zahle, F., Barlas, A., Lønbæk, K., Bortolotti, P., Zalkind, D., Wang, L., Labuschagne, C., Sethuraman,
873 L., and Barter, G.: Definition of the IEA Wind 22-Megawatt Offshore Reference Wind Turbine,
874 Technical University of Denmark, doi:10.11581/DTU.00000317, dTU Wind Energy Report E-0243
875 IEA Wind TCP Task 55, 2024.

876 Zhang, Y., Song, Y., Shen, C., and Chen, N.-Z.: Aerodynamic and structural analysis for
877 blades of a 15MW floating offshore wind turbine, *Ocean Engineering*, 287, 115785, doi:
878 <https://doi.org/10.1016/j.oceaneng.2023.115785>, 2023.

879 Zheng, J., Wang, N., Wan, D., and Strijhak, S.: Numerical investigations of coupled aeroelastic
880 performance of wind turbines by elastic actuator line model, *Applied Energy*, 330, 120361, doi:
881 <https://doi.org/10.1016/j.apenergy.2022.120361>, 2023.